PHYSICAL CONDITIONS IN THE ORION NEBULA AND AN ASSESSMENT OF ITS HELIUM ABUNDANCE

JACK A. BALDWIN,[1,2,3] GARY J. FERLAND,[2,4] P. G. MARTIN,[5] MICHAEL R. CORBIN,[2] STEPHEN A. COTA,[2] BRADLEY M. PETERSON[2] AND ARNE SLETTEBAK[1,2]

ABSTRACT

The Orion Nebula is pivotal in establishing the "dY/dZ relation," which describes both the enrichment of helium as stars produce heavy elements and, from an extrapolation to a condition of no enrichment, the primordial helium abundance. With the goal of redetermining the helium abundance of the Orion Nebula, we have obtained new long-slit spectrophotometric observations. These observations confirm previously noted trends that the density, level of ionization, and emission measure decrease with the distance from the Trapezium. The reddening, measured from ratios of Paschen to Balmer lines, must arise mostly in a neutral sheet in front of the H II region. Most of the hydrogen line emission originates in the ionized flow from the interface between the H II region and the molecular cloud. The observations show that the level of ionization of the gas does not change dramatically across our sampled region; in particular, the ionic abundance ratio He^+/H^+ is nearly constant, with $He^+/H^+ = 0.088 \pm 0.006$. In the bright innermost region the errors are largely dominated by systematic errors due to uncertainties in the reddening curve for Orion grains and deviations from case B emissivity; statistical errors dominate the error budget in the fainter, outer regions.

Photoionization models are computed to determine the correction for the unobserved presence of neutral helium in regions where hydrogen is ionized. We also derive abundances for the heavy elements by comparison with the photoionization model calculations. Emergent continua from newly recomputed Kurucz LTE stellar atmospheres are used as input to the models. The calculations also include a number of important effects of grains on the ionization and thermal structure of the nebula; heating and cooling of the gas by photoemission-recombination from charged grains are found to be substantial. These models reproduce quite well the observed emission-like spectrum, as well as the mid-infrared continuum from the Trapezium region, and show that the correction for neutral helium is small. Our final helium abundance, $He/H = 0.088 \pm 0.006$, is lower than the commonly quoted value because the correction for neutral helium is much smaller than that used in previous work. By comparing our Orion results with solar, stellar, and nebular measurements of helium and heavy-element enrichments, and with the theoretical Y_p from primordial nucleosynthesis, we find that all of the data are consistent with a single line in the Y-Z plane. This is a provocative result for studies of galactic and primordial nucleosynthesis.

Subject headings: nebulae: abundances — nebulae: H II regions — nebulae: Orion Nebula

1. INTRODUCTION

As the H II region with the brightest apparent magnitude, the Orion Nebula has been well studied from X-ray to radio wavelengths (see, for example, Glassgold, Huggins, & Schucking 1982; Goudis 1982). There are two major goals. The first is to determine a phenomenological explanation of the interactions between the stars, the H II region, and the molecular cloud OMC-1. The second goal is to determine the chemical composition of the H II region. Orion has one of the larger oxygen abundances observed among H II regions, and thus helps define relationships between nuclear enrichments of various elements (see Pagel, Terlevich, & Melnick 1986; Peimbert 1986). As well as defining chemical enrichments and deple-

tions in a specific case, Orion also serves as an example of the phenomena likely to occur in other, more poorly studied objects. The situation in other H II regions is likely to be as complicated as it is in Orion (see also Davidson & Kinman 1985, 1990), so that understanding this object has wider application.

In this paper we discuss aspects of both problems, although we are most concerned with the problem of determining the chemical composition of a complicated dusty environment. We emphasize the helium spectrum and the helium abundance, since Orion is pivotal in determining both the slope dY/dZ of the helium–heavy-element abundance enrichment relation, as well as the intercept at zero metallicity, the primordial helium abundance Y_0.

A great deal of previous optical work has centered on the most complicated regions of the nebula, the "bright ridge," the "dark bar," and condensations within the nebula. Here we concentrate on an especially simple region, the direction west of θ^1 Ori C. Section 2 of this paper presents new long-slit spectra covering the region from 30" to 5' from the ionizing star θ^1 Ori C. Radio observations show that the region of greatest emission measure occurs along this axis, 30" west of the star. The observations were mainly aimed at providing accurate helium abundances, and therefore concentrate on

580

measuring the hydrogen and helium spectrum over a wide wavelength range with high photometric precision. This caused us to use low resolution, which somewhat compromised the quality of a few of the heavy-element abundances, but this is shown not to affect the accuracy of the helium abundance determination. In § 3 we investigate the physical conditions indicated by the array of observations. We find several simple correlations along this slit direction: the emission measure falls off according to an inverse square law, the electron density indicated by the [S II] spectrum falls monotonically (but not as a simple power law), and the extinction and level of ionization both decrease. These results point to a simple and plausible geometrical model of at least the western side of the nebula, which is explored in § 4. The geometry adopted is akin to current "blister models" of H II regions in which an ionization front impinges on the molecular cloud and gas flows away from the front at nearly constant pressure, at the sound speed.

Section 5 then develops photoionization models, based on the geometrical model, which allow us to determine in some detail the properties of the innermost, most ionized region we observed. We include explicitly and consistently the effects of dust opacity and of heating and cooling of the gas by photoemission-recombination from charged grains. The predicted spectrum is computed in detail and reproduces with some success the observations, including the continuum spectrum of the infrared Trapezium ("Ney-Allen") nebula. Finally, we use the photoionization model to determine the composition of the nebula, in particular finding a helium abundance ~12% smaller than the currently accepted value. In § 6 we discuss the implications for galactic nucleosynthesis and the primordial helium abundance.

2. OBSERVATIONS

Long-slit observations of the Orion Nebula were obtained at low resolution to study the physical conditions within the gas, and higher resolution observations of θ^1 Ori C were made to study gas lying along the line of sight.

2.1. Long-Slit Observations

Long-slit CCD spectra at identical positions in the Orion Nebula were obtained at two different telescopes: the 1.8 m Perkins Telescope of the Ohio State and Ohio Wesleyan universities at the Lowell Observatory, and later the 4 m telescope at Cerro Tololo Inter-American Observatory (CTIO).

The CTIO data were obtained on the nights of 1988 November 16 and 17 (UT) using the 4 m Ritchey-Chrétien spectrograph with a UV-sensitive GEC CCD. The slit width was 2", while the length was 4.7 divided into 385 pixels of 0.73 each. The slit was placed in an east-west orientation with the easternmost end 30" west of θ^1 Ori C; our data thus extend to about 5' west. A $V \sim 13$ mag fiducial star fell into the slit near its center, and was used to calibrate the position on the sky of all points along the slit. Table 1 summarizes the positions of the synthesized apertures along the slit. A typical spectrum is shown in Figure 1.

Low-resolution (15 Å FWHM) spectra were taken at a blue grating setting on the first night, then a red setting on the second night. The fiducial star allowed us to extract red and blue spectra from exactly the same places on the sky. The combined spectra covered the wavelength range 3650–9720 Å, with a slight overlap at Hα. Flux calibrations were determined independently on each night by observing standard stars

TABLE 1

SLIT POSITIONS, LINE SURFACE BRIGHTNESS, EQUIVALENT WIDTH, AND REDDENING

Slit (1)	$\delta(\theta^1\ C)^a$ (2)	Aperture[b] (3)	$F(H\beta)^c$ ($\times 10^{14}$) (4)	W_λ^d (Å) (5)	$E(B-V)$ (6)
1	37	15.76	99.9	435	0.330
2	45	15.76	132.4	545	0.249
3	53	15.76	110.4	533	0.190
4	61	15.76	81.9	502	0.196
5	69	15.76	73.9	547	0.179
6	76	15.76	60.4	540	0.186
7	84	15.76	42.7	503	0.156
8	92	15.76	41.8	474	0.201
9	100	15.76	22.2	383[e]	0.196
10	108	21.6	18.0	383[e]	0.156
11	133	23.6	16.7	435	0.154
12	145	23.6	17.2	503	0.160
13	157	23.6	14.3	488	0.189
14	173	31.6	10.5	441	0.171
15	189	31.6	8.12	397	0.148
16	204	31.6	7.57	392	0.136
17	220	31.6	7.94	424	0.127
18	236	31.6	6.72	380	0.148
19	252	31.6	5.94	350	0.170
20	268	31.6	4.67	295	0.165
21	291	31.6	4.57	286	0.142

[a] Distance (arcsec) from θ^1 C Ori.
[b] Area of synthesized aperture in arcsec^2.
[c] $H\beta$ surface brightness in ergs cm^{-2} s^{-1} arcsec^{-2}.
[d] Equivalent width of $H\beta$, measured relative to the interpolated continuum at 4861 Å.
[e] Affected by continuum of fiducial star.

through large apertures, but the red spectra were then slightly renormalized to bring their Hα intensities into agreement with those measured in the corresponding blue spectra. On each night we took a series of spectra of widely different exposure times, so that for each of the important emission lines at each point along the slit we would have data which were well exposed but not saturated.

FIG. 1.—Typical spectrum of the Orion Nebula, here the surface brightness at the innermost synthesized slit position (position 1).

The 1.8 m spectra had been obtained previously (on 1988 February 15 UT) with Ohio State University's newly acquired Texas Instruments 4849 virtual phase CCD (format 580 × 390 pixels) mounted on a standard Boller & Chivens spectrograph. The wavelength resolution was 9 Å FWHM, sampled with 4.5 Å pixels. The spectra covered the wavelength range 4125–6750 Å. Calibrating observations and a series of exposures on Orion were carried out in the same way as with the 4 m telescope. The same fiducial star was used as with the CTIO observations, and the slit width was the same, permitting the final extracted spectra to correspond again to the same location on the sky. The detector system was still under development and turned out to have assorted minor problems with linearity, flat-fielding, and bias subtraction which made the data unreliable at the few-percent level. However, since the observations were made under much darker sky conditions and have higher wavelength resolution than the CTIO observations, they have been used to measure the scattered starlight coming from the Orion Nebula and to deblend the [S II] $\lambda\lambda6717$, 6731 doublet. The scattered starlight measurement is only needed to make a small correction for underlying absorption lines (see § 2.3), while the [S II] lines are of nearly equal intensity, so that small linearity problems are not important. Our calibrations were sufficiently accurate for both of these purposes.

2.2. Basic Reductions

The two-dimensional CCD images were reduced using the standard techniques embodied in the IRAF reduction system. Flat-field corrections were carefully determined from the twilight sky (for the 4 m and 1.8 m blue spectra) or from a dome screen, and then checked against twilight sky spectra (for the 4 m red spectra). These calibrations, which affect the intensity ratios as a function of position along the slit, appear to be accurate to about 1% at all pixel locations of interest. The flux calibration was determined from two standard stars on each night for the 4 m data and three for the 1.8 m data; the different stars agreed to an accuracy of 1%–2% over the wavelength range of interest. Before being renormalized the Hα fluxes measured from the CTIO red spectra were on average 5% fainter than those from the CTIO blue spectra, with a 4% rms scatter about this average shift.

We wished to find the intensity ratios of weak lines to strong lines covering a dynamic range of up to several hundred at any given spot along the slit, in a situation in which there was a rapid decrease in the surface brightness of these emission lines outward along the slit. This necessitated a detailed linearity check, which was performed at the 4 m telescope by flashing a constant-current LED light source inside the spectrograph for a series of different precisely controlled times. The CCD's response was found to be linear to within 1% over the full range from the standard background level set by preflashing the CCD with the same LEDs, up to the saturation level.

During data reduction we carefully checked to see which parts of which CCD images were to be avoided because they were saturated. In the case of the blue CTIO data, we eventually used [O III] $\lambda5007$/Hβ and Hα/Hβ intensity ratios measured from one of the shorter exposures in combination with intensity ratios of the weaker lines relative to Hβ measured from a longer exposure.

In the red, Hα and [S III] $\lambda9532$ were saturated on exposures which were long enough for the weakest lines to have high signal-to-noise ratio, so we used a similar technique of measur-

ing intensities relative to intermediate-strength standard lines. However, in place of using just one intermediate-strength line (Hβ) as we did in the blue, we averaged the intensities of three lines: [Ar III] $\lambda7136$, He I $\lambda7065$, and [Ar III] $\lambda7751$. We designate that average intensity as I(intermediate red). A few other lines of similar intensity were not included in this average because of potential problems with blending or overlying telluric absorption. The Hα/(intermediate red) and [S III] $\lambda9532$/(intermediate red) intensity ratios were then measured from a shorter exposure and combined with ratios of all the weaker lines relative to I(intermediate red) measured from a longer exposure. The particular exposures used to measure these various intensity ratios depended on the position along the slit; they were chosen so as to avoid saturation of the lines of interest but to maintain a high signal-to-noise ratio.

The result was that the intensity ratios of weak blue lines to weak red lines depend on multiplying together four different intensity ratios measured from four different exposures. For example, the He I $\lambda5876$/$\lambda6678$ ratio would be found from

$$\frac{I(5876)}{I(6678)} = \frac{I(5876)}{I(H\beta)} \frac{I(H\beta)}{I(H\alpha)} \frac{I(H\alpha)}{I(\text{intermediate red})}$$

$$\times \frac{I(\text{intermediate red})}{I(6678)} . \quad (1)$$

Intensity ratios of blue to red lines are therefore less well measured than ratios for pairs of lines which are both either on the blue spectra or on the red spectra. Accordingly, our analysis technique depends as little as possible on the use of widely separated line pairs.

The CTIO observations were made during dawn twilight. The sky was brightening rapidly during the sequence of exposures, and a sky measurement on a blank field was made only after finishing with Orion. We subtracted the contribution of scattered sunlight in the raw data by scaling our sky measurement so as to remove the strong solar absorption features. The strength of the night-sky Na D lines appeared to increase in step with the amount of scattered sunlight, so that this process also removed that line from the measured spectrum. This is important because blending with Na D would otherwise have added about 10% to the measured strength of He I $\lambda5876$ in the outer parts of the nebula. We believe that our sky subtraction process has adequately corrected for that contamination. On the other hand, we have made no attempt to correct for night-sky contamination of the [O I] $\lambda\lambda5577$, 6300, 6363 emission lines, because we do not have adequate calibrating data.

Another effect of the Earth's atmosphere is that our red spectra are chopped up by the usual strong absorption bands at 6900, 7500, and 9300–9700 Å, plus weaker features at 7200–7300, 8100–8200, and 8900–9200 Å. We removed these in a crude way by using a standard-star spectrum to measure the blended, low-resolution profiles of the absorption bands, and then dividing those profiles into the observed spectra. This allowed us to measure a flux calibration which varied smoothly with wavelength, but it does not deal with the question of whether or not individual sharp emission lines from Orion fall on top of individual sharp absorption lines from the Earth's atmosphere. We checked for the latter problem by comparing the wavelengths of the Orion lines, after all appropriate velocity corrections, with the wavelengths of nearby strong telluric absorption lines. The [S III] $\lambda9069$ line is in fact strongly affected, but [S III] $\lambda9532$ is clear of telluric absorption despite

TABLE 2

RELATIVE LINE INTENSITIES ($H\beta$ = 1.000)

A.

Slit (1)	[O II] $\lambda3727$ (2)	[Ne III] $\lambda3869$ (3)	$H\gamma$ + [O III] $\lambda4350^a$ (4)	$H\gamma$ $\lambda4340^b$ (5)	[O III] $\lambda4363^b$ (6)	He I $\lambda4471$ (7)	C III + $\lambda4652$ (8)	[O III] $\lambda4959$ (9)	[O III] $\lambda5007$ (10)	[O I] $\lambda5577^c$ (11)
1	0.582	0.169	0.443	0.415	0.0119	0.043	0.008	1.222	3.673	0.002
2	0.850	0.147	0.448	0.439	0.0149	0.041	...	1.150	3.449	0.002
3	1.126	0.134	0.451	0.429	0.0121	0.040	0.011	1.036	3.102	0.003
4	1.112	0.139	0.455	0.429	0.0126	0.042	0.013	1.091	3.241	0.003
5	1.061	0.142	0.459	0.424	0.0147	0.041	0.012	1.068	3.211	0.003
6	1.026	0.142	0.461	0.441	0.0132	0.043	0.010	1.066	3.182	0.002
7	0.901	0.154	0.464	0.437	0.0136	0.042	0.010	1.034	3.082	0.004
8	1.084	0.116	0.453:	0.443	0.0121:	0.041	0.013	0.935	2.819	0.004
9	1.008	0.126	0.467:	0.429	0.0102:	0.040	0.011	0.926	2.765	0.007
10	0.911	0.130	0.458	0.479	≤0.016	0.042	0.028	0.917	2.705	0.013
11	1.145	0.112	0.470	0.441	...	0.043	0.014	0.923	2.794	0.009
12	1.161	0.109	0.461	0.429	0.0097:	0.039	0.012	0.915	2.775	0.008
13	1.202	0.092	0.459	0.453	0.0089:	0.043	0.011	0.872	2.603	0.011
14	1.282	0.091	0.468	0.454	0.0109:	0.040	0.013	0.836	2.496	0.014
15	1.374	0.091	0.476	0.483	0.0117:	0.041	0.010	0.764	2.259	0.016
16	1.260	0.087	0.484	0.463	0.0131:	0.040	0.009	0.742	2.202	0.019
17	1.271	0.079	0.469	0.421	≤0.007	0.037	0.014	0.727	2.170	0.017
18	1.297	0.087	0.466	0.427	<0.013	0.036	0.022	0.674	2.024	0.020
19	1.349	0.079	0.474	0.442	≤0.023	0.046	0.030	0.670	2.026	0.027
20	1.406	0.084	0.463	0.439	...	0.042	0.037	0.647	1.973	0.029
21	1.570	0.074	0.485	...	...	0.046	0.042	0.607	1.818	0.031
A_λ^d	7.09	7.00	6.56	6.57	6.54	6.43	6.25	5.95	5.91	5.44

[a] Blend of $H\gamma$ and [O III] $\lambda4363$.
[b] Deblended line intensity.
[c] [O I] blended with night sky.
[d] Extinction at the given wavelength for unit reddening $E(B-V)$. In these units $A_{H\beta}$ = 6.0462.

B.

Slit (1)	[N II] $\lambda5755$ (2)	He I $\lambda5876$ (3)	[O I] $\lambda6300^a$ (4)	[O I] $\lambda6363^a$ (5)	$H\alpha$ + [N II] $\lambda6570^b$ (6)	$H\alpha$ $\lambda6563^c$ (7)	[N II] $\lambda6584^c$ (8)	He I $\lambda6678$ (9)	[S II] $\lambda6725^d$ (10)	[S II] $\lambda6717^c$ (11)
1	0.0117	0.178	0.040	0.008	5.008	4.044	0.603	0.055	0.078	0.025
2	0.0105	0.164	0.034	0.009	4.549	3.856	0.659	0.049	0.072	0.026
3	0.0124	0.152	0.037	0.010	4.703	4.101	0.699	0.042	0.089	0.034
4	0.0097	0.152	0.036	0.011	4.493	3.726	0.737	0.044	0.097	0.041
5	0.0084	0.151	0.030	0.008	4.231	3.632	0.675	0.042	0.088	0.032
6	0.0084	0.152	0.032	0.011	4.235	3.144	0.488	0.043	0.111	0.046
7	0.0068	0.148	0.032	0.010	4.010	3.350	0.531	0.042	0.113	0.048
8	0.0125	0.148	0.043	0.015	4.655	3.590	0.862	0.043	0.158	0.060
9	0.0067	0.147	0.033	0.011	4.343	3.383	0.562	0.045	0.143	0.058
10	...	0.161	0.030	0.016	3.807	3.354	0.468	0.042	0.130	0.059
11	0.0054	0.146	0.029	0.009	3.935	3.274	0.410	0.042	0.122	0.059
12	0.0055	0.146	0.029	0.011	3.992	3.403	0.478	0.044	0.125	0.064
13	0.0050	0.145	0.030	0.012	4.005	3.391	0.544	0.047	0.145	0.074
14	0.0045:	0.147	0.038	0.015	4.277	3.470	0.550	0.045	0.167	0.082
15	0.0050:	0.142	0.041	0.017	4.109	3.265	0.569	0.043	0.160	0.086
16	0.0058:	0.139	0.039	0.015	3.898	3.199	0.475	0.041	0.153	0.083
17	0.0064:	0.133	0.040	0.014	3.967	3.198	0.588	0.043	0.167	0.093
18	0.0054:	0.138	0.043	0.021	3.893	3.199	0.551	0.040	0.174	0.094
19	0.0046:	0.134	0.045	0.024	3.865	3.141	0.491	0.039	0.184	0.101
20	0.0073:	0.138	0.045	0.022	3.749	3.024	0.549	0.036	0.184	0.103
21	0.0097:	0.128	0.053	0.026	3.783	2.768	0.538	0.036	0.211	0.112
A_λ^e	5.30	5.21	4.90	4.86	4.72	4.71	4.70	4.64	4.60	4.61

[a] [O I] blended with night sky.
[b] Blend of $H\alpha$ and [N II].
[c] Deblended line intensity.
[d] Blend of both [S II] lines.
[e] Extinction at the given wavelength, for unit reddening $E(B-V)$. In these units $A_{H\beta}$ = 6.0462.

TABLE 2—*Continued*

C.

Slit (1)	[S II] $\lambda6731$[a] (2)	He I $\lambda7065$ (3)	[Ar III] $\lambda7751$ (4)	H13-3 $\lambda8665$ (5)	H12-3 $\lambda8751$ (6)	H11-3 $\lambda8863$ (7)	[S III] $\lambda9069$[b] (8)	[S III] $\lambda9532$ (9)
1..........	0.054	0.120	0.071	0.022	0.027	0.036	0.660	3.740
2..........	0.046	0.104	0.061	0.017	0.021	0.028	0.496	3.090
3..........	0.068	0.085	0.051	0.015	0.018	0.024	0.401	2.811
4..........	0.072	0.084	0.053	0.015	0.018	0.025	0.395	2.632
5..........	0.064	0.076	0.050	0.014	0.018	0.023	0.399	2.381
6..........	0.078	0.071	0.049	0.015	0.018	0.024	0.436	2.200
7..........	0.072	0.059	0.043	0.013	0.017	0.022	0.430	2.075
8..........	0.108	0.061	0.046	0.016	0.018	0.024	0.484	2.429
9..........	0.091	0.058	0.044	0.016	0.019	0.024	0.469	2.135
10..........	0.087	0.049	0.036	0.014	0.017	0.021	0.367	1.689
11..........	0.069	0.047	0.039	0.014	0.017	0.022	0.313	1.899
12..........	0.073	0.045	0.039	0.014	0.017	0.021	0.305	1.970
13..........	0.083	0.043	0.039	0.015	0.019	0.023	0.370	2.080
14..........	0.094	0.043	0.039	0.014	0.019	0.023	0.357	2.084
15..........	0.086	0.038	0.037	0.014	0.017	0.021	0.299	1.829
16..........	0.079	0.033	0.033	0.014	0.016	0.022	0.291	1.619
17..........	0.085	0.032	0.032	0.012	0.016	0.020	0.280	1.636
18..........	0.090	0.029	0.031	0.015	0.015	0.020	0.255	1.554
19..........	0.087	0.027	0.031	0.015	0.018	0.024	0.229	1.491
20..........	0.091	0.027	0.025	0.013	0.018	0.024	0.228	1.471
21..........	0.100	0.022	0.028	0.013	0.019	0.022	0.263	1.092
A_λ[c]........	4.60	4.36	3.89	3.31	3.26	3.19	3.08	2.84

[a] Deblended line intensity.
[b] Affected by telluric absorption.
[c] Extinction at the given wavelength, for unit reddening $E(B-V)$. In these units $A_{H\beta} = 6.0462$.

being in the middle of a broad absorption band. We therefore use $\lambda9532$ as our measure of the S^{++} abundance (after removing the low-resolution correction for telluric absorption which had previously been applied).

This paper uses intensities for the individual lines in three blends: Hγ + [O III] $\lambda4363$; Hα + [N II] $\lambda\lambda6548$, 6584; and [S II] $\lambda\lambda6717$, 6731. The component intensities were determined by fitting the observed blended profiles with separate components at the predicted wavelengths of the individual lines, each having either the profile of the unblended lines (for the 4 m data) or a Gaussian profile (for the 1.8 m data). The fitted profiles agreed with the observed ones to 5%–10% accuracy. The strength of [O III] $\lambda4363$ is the least certain result from this procedure because it is a weak line on the wing of a much stronger one. Line strengths for the components of this blend and also of the [S II] doublet were determined separately from the data from each telescope. Based on the internal agreement of the low-resolution results and on spot checking against higher resolution data (5 Å and 0.4 Å FWHM), the systematic errors in the intensities of these lines are probably not more than 20%.

The above steps led to a data base of observed line intensities. Table 1 gives the surface brightness of Hβ and of the adjacent continuum for each synthesized aperture. Table 2 presents line intensities relative to Hβ for each aperture along the slit. These surface brightnesses and line ratios have *not* been corrected for extinction (§ 3.1) or underlying absorption (§ 2.3). Table 3 gives the [S II] doublet ratio from the 1.8 m observations.

2.3. *Underlying Absorption*

In addition to the sky background described above, the spectra include a continuum comprised of light scattered from

the Trapezium stars as well as the usual continuum from an ionized gas (recombination and free-free continuous radiation). The scattered component is basically the spectrum of the O6.5 star θ^1 Ori C, modified by a scattering function and falling off sharply as a function of distance outward from the Trapezium. Although the absolute intensity of the continuum falls off sharply, the equivalent width of Hβ is much more nearly constant (see Fig. 2), changing by only about 40% over the length of the slit.

The observed intensities of some emission lines above the continuum are decreased by underlying absorption in the scattered continuum. The intensities of these lines (Hγ, Hβ, and He I $\lambda\lambda4471$, 5876) were corrected as follows. The emission-line equivalent widths, E, were measured directly with the 1.8 m telescope data. We used published values for the stellar absorption-line equivalent widths, A (see Table 4), and used our nebular model (§ 5) to estimate the emission-line equiva-

TABLE 3

[S II] DOUBLET RATIO, PERKINS DATA

Slit (1)	$\lambda6731/\lambda6717$ (2)	Slit (1)	$\lambda6731/\lambda6717$ (2)
1........	1.805	12........	1.159
2........	1.811	13........	1.151
3........	1.739	14........	1.115
4........	1.704	15........	1.052
5........	1.642	16........	0.986
6........	1.613	17........	0.968
7........	1.531	18........	0.934
8........	1.709	19........	0.882
9........	1.477	20........	0.888
10........	1.316	21........	0.831
11........	1.193		
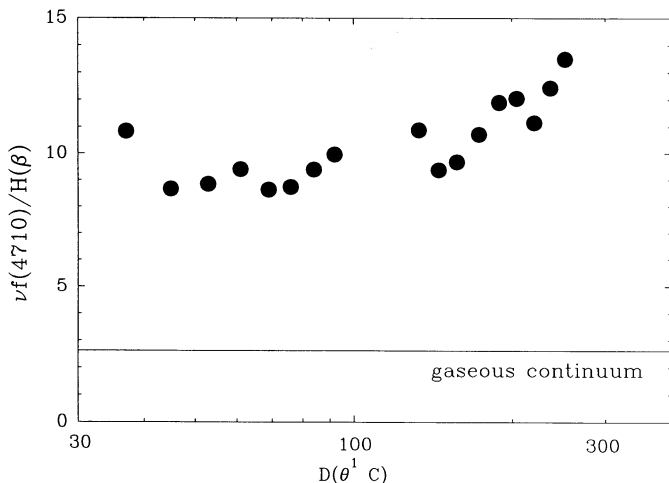
FIG. 2.—Surface brightness of the interpolated continuum at 4861 Å relative to Hβ as a function of offset (arcsec) from θ^1 Ori C. Two points at an offset of $\approx 100''$ are affected by the fiducial star and are not shown. The horizontal line shows the expected level of the gaseous continuum (recombination and free-free continua). The scattered continuum is substantial.

lent width with respect to the gaseous continuum, E_n (also listed in Table 4). Then we multiplied the observed intensities of the emission lines by a factor $(1 + fA/E)$, where $f = (E_n - E)/(E_n + A)$. The final corrections were about 0.5%–1.0% for most lines, but in the 3%–4% range for He I λ4471.

2.4. High-Resolution Observations

Higher resolution observations of θ^1 Ori C were made with the coudé feed telescope at the Kitt Peak National Observatory on 1989 January 9. The TI-3 CCD detector was used with camera 5 and the KPC-007A grating, giving a dispersion of 15 Å mm^{-1} and a resolution of 0.45 Å. The integration time was 30 minutes.

Figure 3 shows the spectrum, with the region around He I λ3889 expanded in the lower panel. The narrow interstellar component of this line appears in absorption against the broad stellar features and continuum of θ^1 Ori C. The lower level of the transition is a highly excited metastable state which is populated following recombination, and so this interstellar absorption line is expected to arise solely in the He$^+$ region of the Orion Nebula unlike the sharp Ca II absorption lines also present in the data, to which the general interstellar medium should contribute. As discussed in § 3.8 below, these lines reveal much about the line of sight to the Trapezium stars.

TABLE 4
ABSORPTION-LINE EQUIVALENT WIDTHS

Line	A^a (Å)	Reference	E_n^b (Å)
He I λ4471	0.56	Conti 1971	88
Hγ	2.5	Conti 1973	932
Hβ	2.5	Auer & Mihalas 1972	1948
He I λ5876	0.68	Conti 1974	256
Hα	0($<$2.5)	Conti 1974	5706
He I λ6678	0($<$0.4)	Conti 1974	73

[a] Equivalent width of the absorption line observed in the stellar spectrum of θ^1 Ori C.

[b] Emission-line equivalent width with respect to the gaseous continuum, estimated using our nebular models (§ 5).
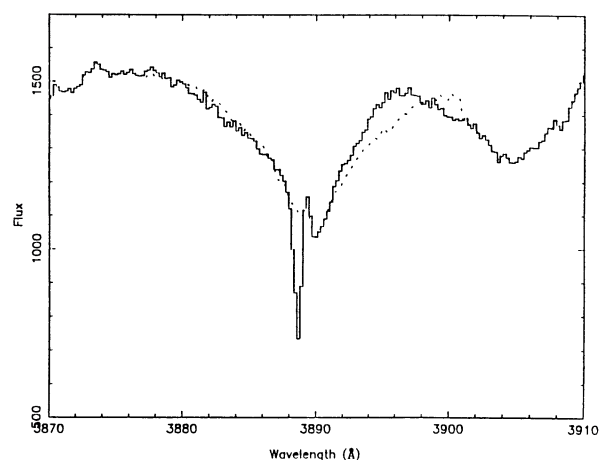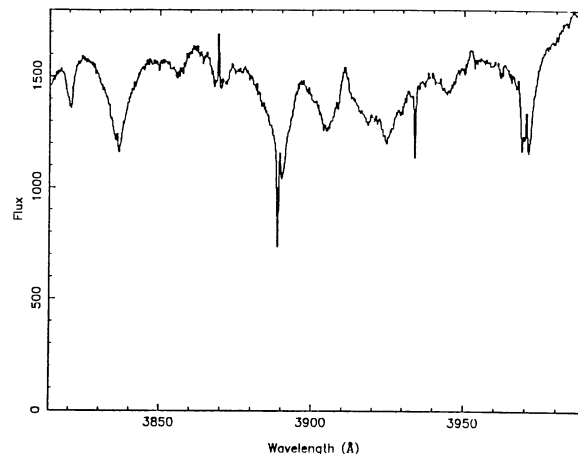
FIG. 3.—Higher resolution observations of θ^1 Ori C are shown. The upper panel shows both broad stellar hydrogen lines and sharper interstellar lines of Ca II and He I. The lower panel shows part of the spectrum on an expanded scale, and the H9 line (dashed) superposed over the H8 line to show the continuum placement for the measurement of the 2 ^3S He I absorption. Uncertainty in continuum placement is the principal source of error in the determination of the absorption-line equivalent width.

The column density of gas in the 2 ^3S level of He^0 can be measured using standard curve-of-growth methods. The curve of growth for λ3889 is shown in Figure 4. It was computed assuming a Doppler parameter of $b = 8.0$ km s^{-1}, suggested by line-width data (Castañeda 1988), and all three line contributions to the multiplet were explicitly included. The measured equivalent width of $W_\lambda(3889) = 0.271 \pm 0.048$ Å corresponds to a deduced column density (cm^{-2}) of log $[N(\text{He I } 2\ ^3S)dl] = 13.90^{+0.35}_{-0.20}$.

3. PHYSICAL CONDITIONS

In this section we deduce the physical quantities that can be found most directly from the observed spectra, without reference to particular geometrical or photoionization models.

The observational setup and the subsequent interpretation were strongly influenced by radio and kinematic studies of the Orion Nebula. As explained in § 4, it appears that as θ^1 Ori C moves into the molecular cloud OMC-1 it carves out a cavity or blister. The observed H II region would be a nearly constant pressure flow away from the H$^+$–H^0 ionization front, which moves into the molecular cloud. Radio and optical observa-
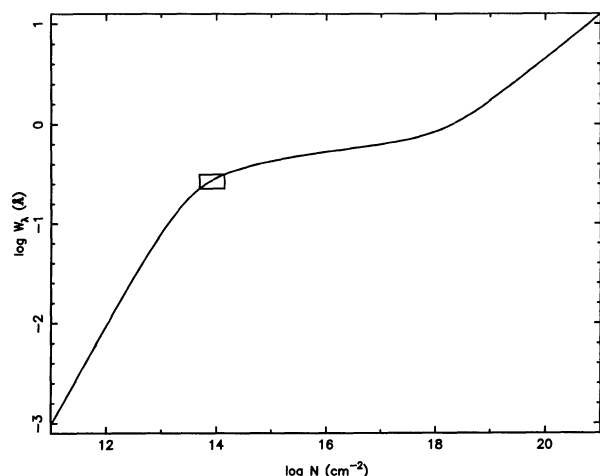
FIG. 4.—Curve of growth for He I λ3889. The rectangle shows the measured equivalent width and the deduced range of column density of the 2 ³S level.

tions agree that the region with largest emission measure occurs some 30″ to the west of θ^1 Ori C.

Our slit was oriented east-west, with the easternmost edge 30″ west of θ^1 Ori C. We show below that along this westerly line extending nearly 5′, the region 30″–40″ from θ^1 Ori C has (a) the greatest emission measure, (b) the largest reddening and (c) the highest level of ionization. This will be the region we consider in the greatest detail in the following analysis.

Various authors quote distances to Orion between 480 and 520 pc; we adopt a distance of 500 pc. The scale along the slit direction is then $100″ = 0.24 \text{ pc} = 7.5 \times 10^{17}$ cm.

3.1. Reddening and Extinction

Before the physical conditions can be assessed, the relative emission-line intensities must be corrected for reddening which arises from both dust along the line of sight to the Orion complex and dust embedded in the nebula. The most reliable way to deduce the effective amount of reddening of the nebular emission involves the detection of widely separated line pairs originating in the same upper level. In this case the intensity ratio is simply related to the branching ratio from the upper level, and does not involve an assessment of the physical conditions within the nebula. Such an approach has been taken by Greve et al. (1989). Even so, there are a number of complications.

3.1.1. Dependence on Geometry

Because of the ionization stratification of the nebula, different lines can originate in different regions of the nebula that suffer different effective reddening. This can be addressed by using as many reddening indicators as possible. Greve et al. (1989) found that [S II] lines, which are formed near the H^+–H^0 ionization front, are more reddened than hydrogen recombination lines. For the extinction law adopted below (which is different from that adopted by Greve et al.) the color excess to the S^+ region is $E(B-V) = 0.47$ mag, while that to a typical point in the H^+ zone is 0.32, very similar to the color excess of θ^1 Ori C, $E(B-V) = 0.32$ mag (Bohlin & Savage 1981). This shows that a typical point in the S^+ region lies at a greater column density than does a typical point in the H^+ zone. Greve et al. do not study the same line of sight as the present work, and cannot separate the hydrogen and sulfur

lines into the components studied by Castañeda (1988; see § 4.1). The location of θ^1 Ori C is discussed further below (§ 4.3).

Our data do not extend to Pγ, so that it is not possible to compare lines produced by the same upper level, as was done by Greve et al. (1989). Rather, the reddening at each position along the slit was determined by using the widest wavelength baseline over which we could reliably measure the hydrogen line spectrum. This involved taking the intensity ratio of Hγ to the Paschen lines at 8665, 8751, and 8863 Å. The predicted case B intensity ratios (Hummer & Storey 1987) vary by only about 4% over the density and temperature range of interest, $N_e \sim 10^3$–10^4 cm^{-3} and $T_e \approx 7500$–10,000 K. In addition, all of these lines originate in fairly high upper levels, and are thus less sensitive to possible internal destruction effects (Cota & Ferland 1988).

Hγ is blended with [O III] λ4363, which is difficult to separate out at our low resolution, but the [O III] line is only a 3%–4% contribution. When determining the reddening at each position along the slit, we subtracted an [O III] contribution determined from the average λ4363/Hγ ratio over the whole slit length, in order to minimize the errors introduced in regions of low surface brightness. As a check for systematic errors in measuring individual Paschen lines, we compared their relative intensities (after correction for reddening) to the predicted values (upper panel of Fig. 5). The average ratios agree with case B to within about 2%, with an rms scatter of about 6%.

The same is not true of the Hα/Hβ decrement, which is shown in the lower panel of Figure 5, after the correction for reddening described below. The intensity ratio is typically 7% below case B predictions. This issue is discussed further in the section on the He^+/H^+ ratio, below.
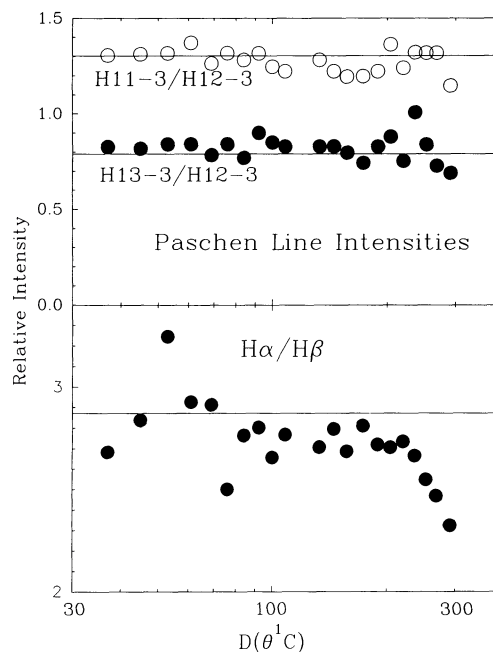
FIG. 5.—Upper panel shows relative intensities of Paschen lines, corrected for reddening, for each synthesized aperture. Case B predictions are indicated by the solid lines. The average ratios agree with case B to within about 2%, with an rms scatter of about 6%. The lower panel shows the reddening-corrected Hα/Hβ intensity ratio. Case B is indicated by the line. The Balmer decrement is significantly below case B predictions.

3.1.2. The Extinction Curve

Another requirement in going from the reddening indicator to the extinction of other lines is the wavelength dependence of the extinction. This might be obtained from the reddening curve for stars. However, the effective extinction for the extended nebular emission need not be identical to that for stars, because nebular light scattered by embedded dust is included in the radiation measured. Extinction is then more dominated by the absorption component, which can have a different wavelength dependence than the sum of absorption plus scattering, the quantity measured from stellar extinction.

Reddening within the Orion Nebula is known to be anomalous. Bohlin & Savage (1981) studied the extinction curve along the line of sight to the Trapezian stars, for which $E(B-V) \sim 0.3$ mag. It is not precisely known where the line-of-sight extinction to even the Trapezium stars originates (but see § 4.3). However, most must originate somewhere within the Orion complex, since Breger, Gehrz, & Hackwell (1981) show that stars more reddened than $E(B-V) = 0.05$ mag and projected on the nebula have anomalous extinction curves like that of the Trapezium rather than like that of the general interstellar medium.

We adopted the Trapezium extinction curve given by Cardelli, Clayton, & Mathis (1989), which has a ratio of total to selective extinction $R \equiv A_V/E(B-V) = 5.5$ (Mathis & Wallenhorst 1981). For each nebular line, the last row of Table 2 gives the total extinction per unit selective extinction $E(B-V)$; the latter is used to parameterize the amount of reddening and extinction on a particular line-of-sight.

For each synthesized aperture, the derived reddening $E(B-V)$ is plotted in Figure 6 and listed in column (6) of Table 1. The values are very similar to those deduced by Greve et al. (1989) for hydrogen lines along a different line of sight. The most important measurement errors in the reddening determination are probably those that arise from linking together the red and blue spectra, which we estimate to be in the 5%–10% range. This would lead to an uncertainty of 0.016–0.032 mag in our estimate below of $E(B-V)$.

3.1.3. Applications

The wavelength dependence of the reddening within the Orion Nebula is known to be anomalous, and we have only the stellar extinction curve to work with in detail. To minimize the dependence of our results on these uncertain corrections, we use the measured color excesses only to correct for selective extinction over the shortest possible wavelength intervals, and to make a correction for total extinction only for near-infrared lines, where the correction is smallest.

For example, we measured the He^+/H^+ ionic ratio only from He/H line pairs which are close together in wavelength, eliminating the direct uncertainties of linking the red and blue spectra. There is a small residual uncertainty relating to the reddening correction, which is based on the linked spectra. We also redetermined the key He/H intensity ratios (see § 3.6) in the extreme case of using the " standard " interstellar extinction curve (Savage & Mathis 1979). Although the deduced $E(B-V)$ is different, the individual intensity ratios change by less than 7%, but with different signs, so that the average change is less than 2%. Combining all of these effects, the quantifiable uncertainty in the final corrected He/H intensity ratios is 5% or less. There still might be additional systematic errors arising because the different emission lines are formed in different zones within a dusty medium that is strongly scattering, and
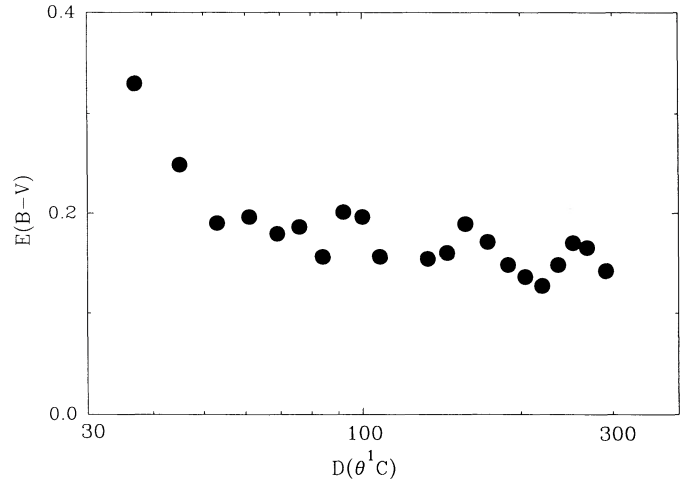
FIG. 6.—Reddening at each synthesized aperture, as deduced from the ratio of Paschen to Hγ lines. The foreground reddening is known to be small [$E(B-V) = 0.05$; Breger et al. 1981], so that most of the reddening shown here originates within the Orion complex.

because of fundamental uncertainties in the actual form of the extinction curve. We have no way of estimating the size of these effects, and in fact we shall see below that this poses a fundamental uncertainty in interpreting our spectra.

3.2. The [S II] Density

The electron density N_e in the H^+ and He^+ zone must be determined for (at least) two reasons: for assessing the amount of collisional excitation of the helium lines (Clegg 1987) and for converting emission measure to physical thickness.

The only candidate density indicator in our data set is the near-infrared [S II] doublet $\lambda\lambda 6717, 6731$ (Osterbrock 1988). N_e was found using calculations for a five level atom, assuming a temperature of 10^4 K (the results depend only weakly on this assumption). Collision strengths of Mendoza (1982) and transition probabilities of Mendoza & Zeippen (1982) were used. Deduced densities are given in column (5) of Table 5. Figure 7
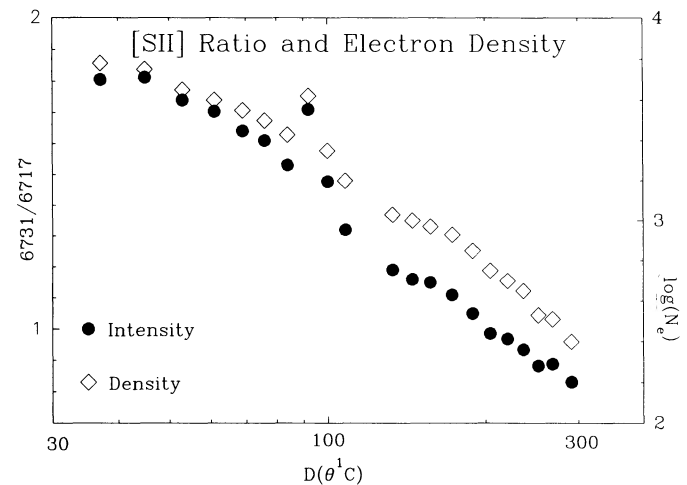
FIG. 7.—Observed [S II] line ratio and deduced electron density. Filled symbols show the intensity ratio $I(6731)/I(6717)$, as measured from the higher resolution Perkins observations (scale on left vertical axis). The density deduced from this ratio (open symbols; right vertical axis) is a lower limit to the density in the H^+ zone of the nebula, because S^+ can exist in regions which are predominantly neutral.

TABLE 5
DEDUCED QUANTITIES

Slit (1)	Distance[a] (2)	$T([N\ II])^b$ (3)	$T([O\ III])^c$ (4)	$N_e([S\ II])^d$ (5)	$\int N_e N_{H^+} \epsilon\, dl^e$ (6)
1.........	2.77(17)[f]	1.17(4)	0.87(4)	60.(2)	2.73(25)
2.........	3.37(17)	1.06(4)	0.93(4)	56.(2)	2.21(25)
3.........	3.96(17)	1.09(4)	0.89(4)	45.(2)	1.33(25)
4.........	4.56(17)	0.97(4)	0.89(4)	40.(2)	1.05(25)
5.........	5.16(17)	0.94(4)	0.93(4)	35.(2)	8.27(24)
6.........	5.68(17)	1.07(4)	0.91(4)	32.(2)	7.20(24)
7.........	6.28(17)	0.95(4)	0.92(4)	27.(2)	4.27(24)
8.........	6.88(17)	1.00(4)	0.92(4)	42.(2)	5.21(24)
9.........	7.48(17)	0.93(4)	0.88(4)	22.(2)	2.72(24)
10.........	8.08(17)	...	≤1.00(4)	16.(2)	1.72(24)
11.........	9.95(17)	0.96(4)	...	11.(2)	1.66(24)
12.........	1.08(18)	0.91(4)	0.84(4)	10.(2)	1.66(24)
13.........	1.17(18)	0.85(4)	0.86(4)	9.3(2)	1.65(24)
14.........	1.29(18)	0.81(4):	0.92(4)	8.8(2)	1.15(24)
15.........	1.41(18)	0.83(4):	0.96(4)	7.1(2)	7.57(23)
16.........	1.53(18)	0.93(4):	1.00(4)	5.6(2)	5.14(23)
17.........	1.65(18)	0.89(4):	≤0.85(4)	5.0(2)	6.63(23)
18.........	1.77(18)	0.86(4):	<1.03(4)	4.5(2)	5.97(23)
19.........	1.88(18)	0.85(4):	≤1.25(4)	3.4(2)	6.75(23)
20.........	2.00(18)	...	...	3.2(2)	5.23(23)
21.........	2.18(18)	...	...	2.5(2)	4.39(23)

[a] Projected distance (cm) from θ^1 Ori C, for an assumed distance of 500 pc.
[b] Temperature deduced from [N II] $\lambda\lambda5755, 6584$ ratio.
[c] Temperature deduced from [O III] $\lambda\lambda4363, 5007$ ratio.
[d] Electron density deduced from [S II] $\lambda\lambda6725, 6717$ ratio.
[e] Emission measure (cm^{-5}) deduced from H11-3.
[f] In compact notation this represents 2.77×10^{17}.

shows both the line ratio and N_e. The well-known Orion density gradient is apparent (see also Osterbrock & Flather 1959).

Unfortunately, [S II] is not a direct indicator of the density of the fully ionized zone. Under normal circumstances, [S II] lines arise in both the H^+ and H^0-C^+ regions of the nebula, because the ionization potential of S^0 is low, 10.36 eV. As a result, [S II] can be formed in regions which are only partially ionized, and the electron density indicated by the doublet ratio is actually a lower limit to the electron density in the adjacent H^+ zone. This happens despite the tendency in a constant pressure flow for the hydrogen nucleon density N_H to be highest in cooler, neutral regions (see also Mihalszki & Ferland 1983). The photoionization calculations for the innermost slit position presented below illustrate this effect; three observed line ratios are density sensitive; [N II] $\lambda5755/\lambda6584$, [O II] $\lambda3727/\lambda7325$, and the [S II] doublet. The best overall fit to these lines required a mean electron density in the H^+ zone of 9.6×10^3 cm^{-3}, while the [S II] spectrum by itself suggested a density a factor of 0.63 smaller, ~ 6000 cm^{-3}. The infrared [S III] fine-structure lines offer in principle a better density indicator, since this is the dominant ion (Table 10). Recent observations of [S III] (Megeath et al. 1990) indicate that $N_e > 6000$ cm^{-3} near the emission-measure peak, which is consistent with the above results. Further support for a high density comes from the [O III] fine-structure lines (Rubin et al. 1988). However, we caution that these infrared measurements do not correspond to the exact spot in the nebula which we have studied.

3.3. The [O III] Temperature

Figure 8 shows the observed and reddening-corrected ratio $r_0 \equiv I(4364)/I(5007)$, a well-calibrated thermometer valid for

densities $N_e \ll 7 \times 10^5$ cm^{-3} (Osterbrock 1988). The densities are observed to be substantially below this value, and so we adopt r_0 as the primary temperature indicator. To calibrate r_0 we used collision strengths from Burke, Lennon, & Seaton (1989) and transition probabilities from Nussbaumer & Storey (1981). The temperature scale is provided in Figure 8. Column (4) of Table 5 gives deduced temperatures for each slit position.

Figure 8 shows that, within the error bars, the dereddened value of r_0 is constant. Within 100" of θ^1 Ori C, where the ratio
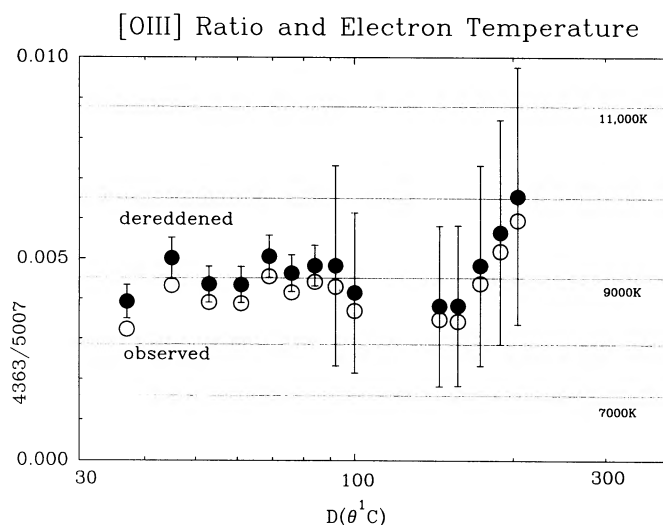
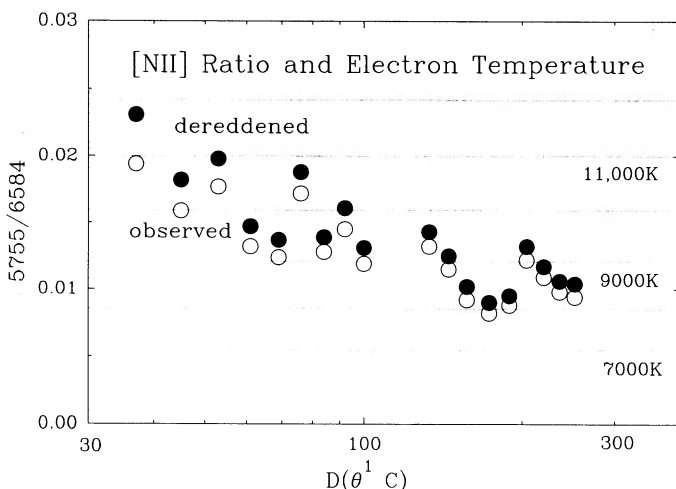FIG. 8.—Observed and reddening-corrected intensity ratio ratio $I(4363)/I(5007)$ as a function of slit position, with th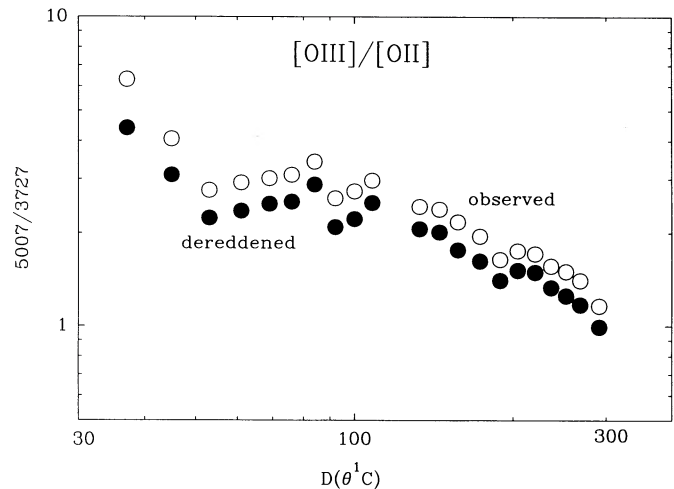e temperature calibration indicated by the horizontal lines. The data are consistent with a constant temperature of 9030 ± 200 K.

is best determined, the mean value is $r_O = (4.6 \pm 0.4) \times 10^{-3}$. This corresponds to a temperature $T(O^{++}) = 9030 \pm 200$ K. This is in excellent agreement with previous optical (Bohuski, Dufour, & Osterbrock 1974; McCall 1979) and radio (Wilson & Pauls 1984) measurements. Since neither our data nor these other measurements suggest the presence of a temperature gradient in the O^{++} zone of the nebula, we assume a constant temperature of $T(O^{++}) = 9000$ K in the following analysis.

3.4. The [N II] Temperature

Figure 9 shows the [N II] ratio $r_N \equiv I(5755)/I(6584)$, another familiar temperature indicator. The ratio r_N has greater uncertainty than the corresponding [O III] ratio because the lines are weaker. An interesting result is the increase in r_N at the smallest offsets where the nebula is brightest and the spectrum is especially well measured.

The temperature calibration, in the limit of low density, is given on the figure, while column (3) of Table 5 gives the deduced temperature in the N^+ zone. The indicated rise in temperature to above 10^4 K in the regions of the nebula closest to θ^1 Ori C might be exaggerated because the [N II] spectrum and hence the temperature calibration can be affected by collisional de-excitation. The critical density for the [N II] nebular lines is $\sim 9 \times 10^4$ cm^{-3}, nearly an order of magnitude lower than that of [O III]. The ionization potentials suggest that N^+ occurs in the H^+ regions of the flow. As discussed above, this region is likely to have electron densities above that indicated by the [S II] ratio, which already rises to $N_e \sim 6000$ cm^{-3} for slit positions closest to θ^1 Ori C. Photoionization calculations presented below, which reproduce the observed [N II] spectrum, confirm this effect of density.

There is a tendency for the O^+–N^+ zones of a nebula to be hotter than the O^{++} zone because of the hardening of the incident radiation field due to photoelectric absorption. Thus, in general, the [N II] spectrum should indicate a higher temperature than the [O III] spectrum. The tendency for the density to increase at smaller offsets further increases the deduced temperature.

3.5. The Ionization Gradient

The observed and reddening corrected ratios [O III] $\lambda5007/$ [O II] $\lambda3727$ and [S III] $\lambda9532/$[S II] $\lambda6725$ are plotted as a

FIG. 10.—[O III]/[O II] intensity ratio, observed and reddening-corrected, as a function of slit position.

function of slit position in Figures 10 and 11, respectively. A gradient is observed in both cases. At the innermost slit positions, transitions from both singly ionized species are affected by collisional de-excitation (these are density indicators), accounting for roughly half of the change observed in the above ratios. The remainder appears to reflect a physical ionization gradient, with the gas nearer (at least in offset) the source of ionizing radiation (θ^1 Ori C) more highly ionized.

3.6. The He^+/H^+ Ionic Abundance Ratio

Lines of hydrogen and helium can be used to determine the He^+/H^+ ionic abundance ratio with some precision, if the lines are formed by radiative recombination and their intrinsic intensities can be determined. Then the conversion from line intensity ratios into ionic abundances is by a simple scale factor. We use effective radiative recombination coefficients from Hummer & Storey (1987) and Brocklehurst (1972). The latter have recently been recomputed by Smits (1990), who generally finds excellent (few-percent) agreement. We assume a constant temperature of 9000 K, as indicated by the [O III] spectrum.

FIG. 9.—Observed and reddening-corrected intensity ratio $I(5755)/I(6584)$ as a function of slit position, with the (low-density) temperature calibration indicated by the horizontal lines.
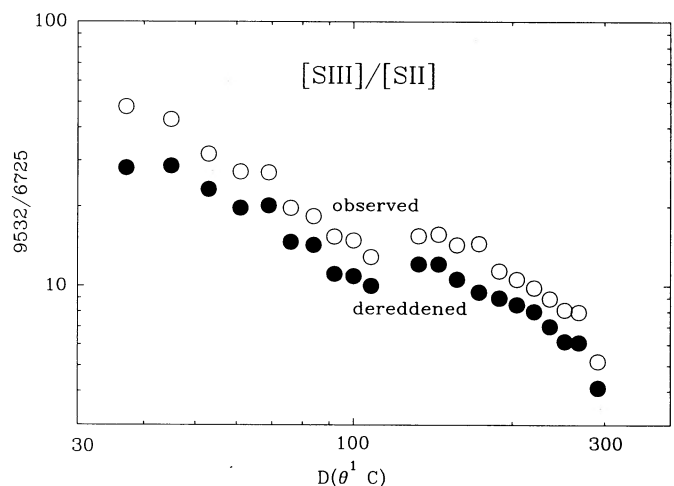
FIG. 11.—[S III]/[S II] intensity ratio, observed and reddening-corrected, as a function of slit position.

The Orion Nebula is exceptionally dense by H II region standards. As a result a correction for a collisionally excited contribution to the helium lines must be made (see, for example, Clegg 1987). We adopted a constant temperature of 9000 K again, together with the density indicated by the [S II] doublet ratio, and the expressions given by Clegg. The correction for collisions is not great and is somewhat uncertain. On the one hand, the models of the innermost slit positions described below show that Lyα photoionization of the helium metastable 2 ^3S level depresses the level population by $\sim 23\%$ below that expected from collisional and radiative decays alone; this effect should diminish with increasing offset. On the other hand, the density deduced by the models is actually higher than the [S II] spectrum alone suggests. These two effects should largely compensate for each other. The suggestion that charge transfer can affect the level population of He I 2 ^3S is discussed in Appendix B.

Several He–H line pairs can be measured with the present data. Our selection was governed by minimizing the large and uncertain correction for reddening which must be applied, and the possibility of deviations from case B hydrogen emissivity. It is also potentially advantageous to pair lines of comparable intensity, although, as discussed, the detector is very linear. Among the helium lines, the He I λ4471 line appears to be the preferred abundance indicator because the correction for collisional excitation is smallest (the correction for underlying absorption is, however, greatest). Of the various line ratios, λ4471/Hγ has virtually no dependence on the reddening correction. Hγ is slightly sensitive to the removal of [O III] λ4363, but this is in total only a few-percent correction. The deduced ionic ratios from this line pair are shown as a function of slit position in Figure 12. Table 6 summarizes the ionic abundance broken down into three spatial groups; the innermost 90″, the data between 90″ and 240″ (data outside this radius are unacceptably noisy), and, finally, both groups together. These indicators, and radio and optical data discussed below, are compared in Figure 13. The errors quoted in Table 6, Figure 13, and below represent the rms scatter among the data for the different slit positions. If this scatter for each ratio represents random measurement errors, the *error in the mean* would be
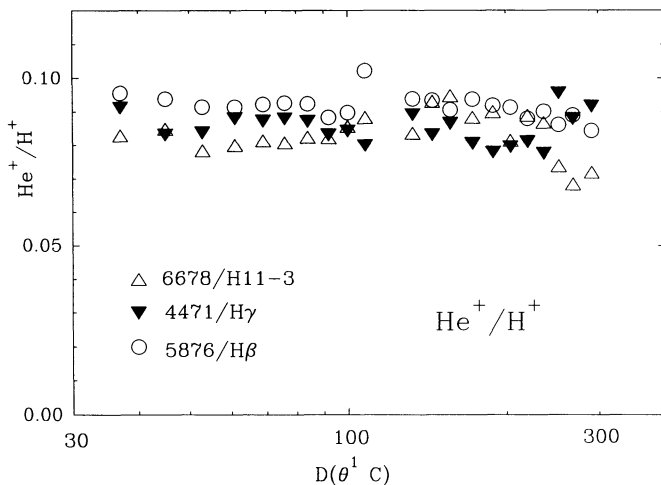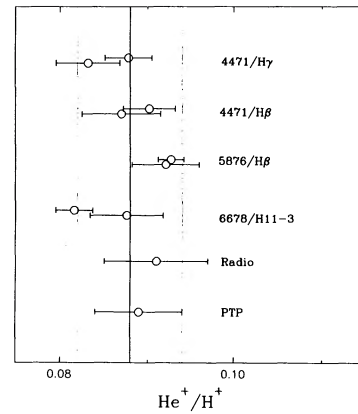
FIG. 13.—Various indicators of the ionic helium abundance are shown, together with our mean and uncertainty. The two points for each of the upper four line ratios correspond to means measured in regions with offsets less than (the higher of the two) and greater than (the lower) 90″. The radio data are from Peimbert et al. (1988), and the point marked PTP is from Peimbert & Torres-Peimbert (1977) and is for a different position in the nebula, centered 27″ south of θ^1 Ori C.

smaller, by the square root of the number of slit positions (7, 11, and 18 for the three groups, respectively).

Hβ is another favorable line to pair with λ4471. The reddening correction is larger, typically 5%–10%. As shown in Table 6 and Figure 13, in the innermost 90″, where the signal-to-noise ratio is greatest, the two line ratios λ4471/Hβ and λ4471/Hγ are in good agreement (another way to cast this is to say that the reddening-corrected Hγ/Hβ is close to case B). In the innermost 90″ the two line ratios indicate $He^+/H^+ = 0.089 \pm 0.003$, and the mean over the next entire 240″ is 0.087 ± 0.004. We adopt $He^+/H^+ = 0.088 \pm 0.004$.

As a check, the deduced ionic ratios for two other line pairs, λ5876/Hβ and λ6678/H11-3, are shown in Figure 12. It is clear from inspection of the figure that in the innermost 90″ the differences in the abundances indicated by the various line ratios are greater than the individual standard deviations would suggest, so that there must be some systematic error. It seems likely that this could be attributed to uncertainty in the exact form of the correction for reddening (§ 3.1).

The λ5876/Hβ and λ6678/H11-3 ratios are both far more sensitive to the reddening correction than the λ4471 ratios discussed above; in the innermost regions typical reddening corrections are $\sim 20\%$ and $\sim 35\%$, respectivley. The ionic ratios given in Table 6 were deduced assuming a smoothed extinction curve as parameterized in terms of R by Cardelli et al. (1989); we used their value of $R = 5.5$ for θ^1 Ori C. The actual extinction to three Trapezium stars is reported by Cardelli & Clayton (1988). For the $E(\lambda 5876 - H\beta)$ differential extinction, the typical scatter among the Trapezium stars is about 0.1 mag [on a scale where $E(B - V) = 1$]; whether this reflects a difference along closely adjacent lines of sight, or, as

FIG. 12.—He^+/H^+ ionic abundance ratio as a function of slit position. The ionic abundance ratios are estimated from the reddening-corrected intensity ratios λ5876/Hβ, λ4471/Hγ, and λ6678/H11-3. Case B, with a correction for collisional excitation of the helium lines, is assumed.

TABLE 6

He^+/H^+ ABUNDANCE INDICATORS

Lines	30″–90″	90″–240″	30″–240″
λ4471/Hγ	0.0878 ± 0.0027	0.0832 ± 0.0036	0.0855 ± 0.0040
λ4471/Hβ	0.0902 ± 0.0030	0.0870 ± 0.0045	0.0886 ± 0.0043
λ5876/Hβ	0.0927 ± 0.0015	0.0921 ± 0.0039	0.0924 ± 0.0031
λ6678/H11-3	0.0816 ± 0.0021	0.0876 ± 0.0042	0.0852 ± 0.0046
All lines	0.0876 ± 0.0047	0.0868 ± 0.0042	0.0880 ± 0.0057

seems more likely, is merely a measure of the observational uncertainty of the pair method of deriving reddening, is a moot point, since in either case there must be this much uncertainty in the curve that we wish to apply. For $E(B-V) \sim 0.3$, this would lead to a few-percent uncertainty in the ionic abundance ratio. The smooth parameterized curve we used in fact systematically underestimates the observed differential extinction by about the same amount, 0.1 mag. This would make our abundance estimate from this line ratio systematically high by a few percent (0.003), accounting for the difference between the mean ionic abundance indicated by $\lambda5876/H\beta$ (0.092 ± 0.003) and $\lambda4471$ relative to $H\beta$ or $H\gamma$ (0.088 ± 0.003). The observational data shown by Cardelli & Clayton do not cover the baseline needed for the $\lambda6678/H11$-3 ratio, so that it is not possible to judge how precise the smoothed reddening law is for this line pair, but we cannot expect it to be better than for $\lambda5876/H\beta$.

Another variant is that in this nebular geometry scattered light will be recovered in the beam, so that we should use a curve more like the absorption component rather than the total extinction. Since the albedo in the optical increases with energy for the size ranges considered, the absorption would be even flatter than the extinction. Preliminary assessment of this effect suggests that the lines ratios would be brought into closer agreement with $\lambda4471/H\gamma$ (which is fairly insensitive to this effect).

$H\alpha$ is not used in any line pair for abundance purposes, despite the fact that the $\lambda6678/H\alpha$ intensity ratio would have little dependence on reddening. As mentioned in § 3.1, the reddening-corrected $H\alpha/H\beta$ ratio (Fig. 5) does not have the case B value, indicating either that the reddening correction is imperfect or that the Balmer decrement is not described by case B. One way to address this puzzle is to examine the ionic helium abundance that would be implied by the $\lambda6678/H\alpha$ intensity ratio assuming case B. The resulting ionic abundances were systematically higher than those indicated by the other line pairs ($He^+/H^+ = 0.0986 \pm 0.0096$ and 0.1057 ± 0.0045 for the $30''$–$90''$ and $90''$–$240''$ averages, respectively, and 0.1029 ± 0.075 for the grand average), suggesting that $H\alpha$ does have an intrinsic emissivity that is too small. The model calculations presented below confirm that $H\alpha$ does have an emissivity below case B predictions. This is to be contrasted with $H\beta$ and $H\gamma$, both of which indicate similar He^+/H^+ ratios (Table 6).

Figure 13 compares the ionic abundance indicators discussed above. For the reasons discussed, we feel that the $\lambda4471/H\gamma$ ratio is the most reliable. More conservatively, but subjectively, if we give high weight to data for $\lambda4471$ relative to $H\beta$ and $H\gamma$ but include the other ratios, we are lead to $He^+/H^+ = 0.088 \pm 0.006$, where the increased error bars (from 0.003) are an acknowledgment of the presence of systematic errors. Figure 13 also shows this mean and uncertainty; the other line ratios checked seem consistent with this range. Alternatively, if we simply give equal weight to each ratio in Table 6, the mean abundance indicated by the entire data set is $He^+/H^+ = 0.0880 \pm 0.0057$ (Table 6); again the quoted uncertainty is conservative, reflecting the scatter in the data rather than the standard deviation of the mean. Because of offsetting responses of the different line ratios to changes in the reddening correction, this mean value is much less sensitive than the individual ratios. Again, the conservative uncertainty is larger than from $\lambda4471/H\gamma$ alone.

Figure 13 also includes the results from radio observations of Peimbert et al. (1988) and from the optical observations of

Peimbert & Torres-Peimbert (1977), both for the position $0''.45$ south of θ^1 Ori C. Their He^+/H^+ ratio is in quite good agreement with our results. However, this must nevertheless be something of a coincidence, given the different corrections for reddening, self-absorption, and collisional excitation that they adopted. Uncertainties associated with radio recombination lines are discussed in Appendix A.

To convert the observed He^+/H^+ ratio to the true He/H ratio, it is necessary to determine whether a correction for the unobserved presence of neutral helium in the H^+ zone of the nebula is needed (see Osterbrock 1988), and whether dust mixed with the ionized gas can diminish the emissivity of the hydrogen lines. These are critical steps in this and any other paper concerning nebular helium abundances. A model of the nebula must always be brought into play, whether it is explicitly calculated or is embedded in some ionization correction scheme. In the present case, no significant trend in the ionic abundance ratio with slit position is apparent, suggesting that neither correction is large. Photoionization models are presented in § 5 to investigate these corrections further, and to determine the abundances of the other elements. A prerequisite to this is to have some idea of the overall geometry of the nebula, in terms of both its gas and dust components.

4. GEOMETRY

4.1. Overview

Kinematic studies are powerful probes of spatial structure, and many papers have been devoted to unraveling the geometry of the Orion Nebula (see, for example, Zuckerman 1973; Balick, Gammon, & Hjellming 1974; Dopita, Dyson, & Meaburn 1974; Pankonin, Walmsley, & Harwit 1979; Balick, Gull, & Smith 1980; Goudis 1982; Simpson & Rubin 1984). The picture we envision is based on these. The star θ^1 Ori C is on the near side of the molecular cloud OMC-1 and is moving into it with a relative speed of ~ 3 km s^{-1}, carving out a cavity or blister. In this case the observed H II region is a nearly constant-pressure "champagne" flow toward us, away from the H^+–H^0 ionization front which moves into the molecular cloud. Recent support for the blister champagne flow model comes from the pattern of the radial velocity of optical lines across the face of the nebula (Castañeda 1988), from the ionization structure dependence of the radial velocity (Hänel 1977), and from studies of H I absorption (van der Werf & Goss 1989) and [C II] 158 μm emission (Boreiko, Betz, & Zmuidzinas 1988) from the transition zone between the ionized gas and the molecular cloud.

Castañeda (1988) studied structure within the [O III] $\lambda5007$ line profile across much of the Orion Nebula. Near θ^1 Ori C along the east-west line the emission line had two strong components with heliocentric velocities ~ 15–20 km s^{-1} (component A) and 8–14 km s^{-1} (component B). Component B tends to be weaker than A. A third, higher velocity (~ 20–40 km s^{-1}) broad component was much weaker. (Note that all velocities cited here will be heliocentric; subtract 18 km s^{-1} to transform to the local standard of rest.) In the context of the champagne flow, Castañeda identifies component A as the gas flowing from the background molecular cloud–H II region interface and interacting with a bubble around the star, and the somewhat fainter component B as gas located closer to us in the flow, so that there are two distinctly different emission-line regions contributing to the observed spectrum. We present evidence in § 4.4 below suggesting that θ^1 Ori C is between two

sheets of ionized gas, and further argue that a substantial fraction of the reddening occurs in neutral material on this side of the H II region.

4.2. *Geometrical Constraints from the Emission Measure*

The absolute surface brightness in the hydrogen lines provides clues to the geometry of the emission-line regions. Tables 1 and 2 give the surface brightness of $H\beta$ and the intensities of several Paschen lines relative to $H\beta$. The surface brightness of a recombination line is given by

$$F(\lambda) = \int j(\lambda, T_e) N_e N^+ \epsilon \, dl , \qquad (2)$$

where $4\pi j(\lambda, T_e)$ is the effective emissivity of the transition wavelength (Hummer & Storey 1987) and ϵ is the filling factor (Osterbrock & Flather 1959). We chose to analyze the 11-3 Paschen line because it is strong and fairly well measured, and because it lies in the near-infrared and is least affected by extinction.

Figure 14 shows the observed and reddening-corrected surface brightness of the line. Empirically, the reddening-corrected surface brightness falls off according to an inverse square law:

$$F(\text{H11-3}) = 1.3 \times 10^{-14} (D/100)^{-2} \text{ ergs cm}^{-2} \text{ s}^{-1} \text{ arcsec}^{-2} , \qquad (3)$$

where D is the offset in arcseconds from θ^1 Ori C. In a geometry which is optically thick to ionizing radiation (radiation-bounded) the surface brightness in a recombination line is simply proportional to the incident flux of ionizing photons, in the absence of dust absorption, if we observe normal to the surface. The observed inverse square law dependence of the surface brightness on D then suggests that δr, the separation between θ^1 Ori C and the wall of the blister, is small compared with D (col. [2] of Table 5). Thus $\delta r < 3 \times 10^{17}$ cm (0.1 pc), very similar to the value deduced by Schiffer & Mathis (1974). This is not correct in detail, of course, since there would also be a cos θ effect in the flux for a flat slab.

The density also decreases with increasing projected slit distance (Fig. 7), but not as rapidly as D^{-2}. In this case the ioniza-
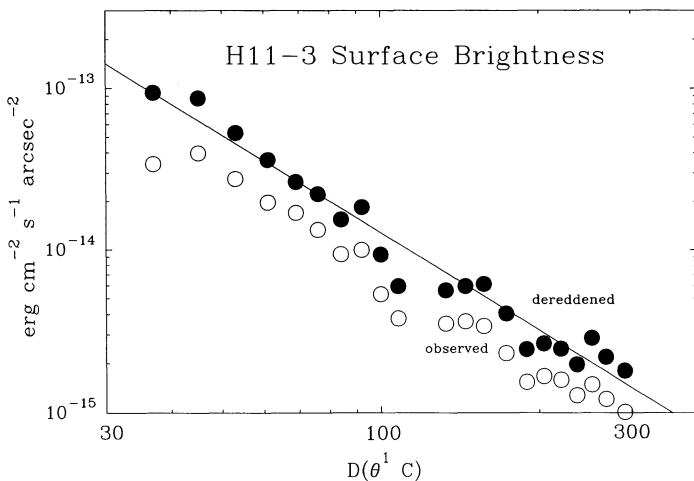
FIG. 15.—Physical extent of the H^+ zone along the line-of-sight, deduced from the H11-3 emission measure and the corrected [S II] density, as described in the text. Note the linear scale.

tion parameter, which is proportional to the ionizing photon density divided by the total hydrogen density, will decrease outward along the slit. This accounts qualitatively for the observed change in the level of ionization of the gas, as indicated by the oxygen and sulfur spectra (Figs. 11 and 12).

The deduced value of the emission measure, $\int N_e N_{H^+} \epsilon \, dl$, is given in column (6) of Table 5. From the emission measure we can estimate the effective physical extent of the hydrogen ionized zone *along the line of sight*, $\int \epsilon \, dl$, by using the density indicated by the [S II] spectrum, after correcting for the fact that this density indicator falls consistently low, as suggested by the photoionization models discussed below. For the specific model described in the following section, the [S II] ratio indicates a density of 6000 cm^{-3}, while the best-fitting model had a density in the H^+ zone which was roughly 50% higher. We convert the observed emission measure into an inferred column density by assuming that this same scale factor holds across the nebula. Figure 15 shows the extent of the ionized zone as a function of projected distance from θ^1 Ori C. The correction to the density described above is model-dependent and hence uncertain. Also, recall that the kinematic data of Castañeda (1988) show that there are actually three distinct gas components along the line-of-sight. Therefore, it is not possible to determine the detailed distribution of the gas along the line of sight from our data alone; Figure 15 is at most just a sketch of the true situation. However, we note that, together with the small deduced δr between the star and the blister, this simplified treatment of the data suggests a geometry which is very reminiscent of those predicted by blister models of H II regions (see especially Fig. 3 of Yorke 1986).

The blister (or background slab) geometry can be contrasted to a (hemi)spherical geometry centered near θ^1 Ori C, in which one would expect that the thickness derived in the radial direction would correspond to the size of the nebula projected on the sky ($>15'$, or 7×10^{18} cm). To reproduce the present observations with this model one would require a small filling factor ϵ which increased outward from θ^1 Ori C. (In rejecting a flattened geometry as implausible, Osterbrock & Flather 1959 derived a small filling factor for a spherical model, but with no spatial resolution.) The [S II] density gradient is also not easily

FIG. 14.—Observed and reddening-corrected H11-3 surface brightness (ergs cm^{-2} s^{-1} arcsec^{-2}) as a function of slit position. The solid line is the inverse square law fit described in the test.

reconciled with a filled sphere with a strong density gradient, since [S II] emission arises near the ionization front. However, models with optically thick clumps (e.g., Schiffer & Mathis 1974) might be possible if the internal density of the individual clumps were arranged to decrease away from θ^1 Ori C. This seems to us somewhat ad hoc; one would certainly want to understand why such a structure would develop during the dynamical evolution of the complex.

4.3. Dust and Column Density

4.3.1. Visual

To relate visual extinction and hydrogen nucleon column density, we adopt

$$\frac{A_V}{\int N_H dl} \approx 5.3 \times 10^{-22} \text{ mag cm}^2 \, , \qquad (4)$$

which holds for the diffuse interstellar medium (Savage & Mathis 1979). Following Cardelli et al. (1989), this ratio might be a slight overestimate for regions of higher R, like Orion. However, we expect this ratio to be less dependent on grain anomalies than is the value of R: the total amount of extinction at visual (and longer) wavelengths is apparently less dependent on the actual grain-size distribution than is the selective extinction $E(B-V)$.

4.3.2. Ultraviolet

The Orion stellar extinction is very gray in the ultraviolet by interstellar medium standards. Typically $A_{UV} \approx 2A_V$, where 1300 Å $\leq \lambda_{UV} \leq$ 3000 Å (Bohlin & Savage 1981). This is a factor 2–3 smaller than is found in the general interstellar medium. Both the large value of R and the gray UV opacity suggest that the mean grain size within the Orion complex is relatively large (Breger et al. 1981; Mathis & Wallenhorst 1981; McCall 1981), which is related to a deficiency of small grains (Cardelli et al. 1989; Martin & Whittet 1990).

Then from equation (4) the ultraviolet opacity (scattering plus absorption cross section per hydrogen nucleon) is given by

$$\sigma_{UV} \approx 1 \times 10^{-21} \text{ cm}^2 \, . \qquad (5)$$

This is consistent with an albedo of $\sim\frac{1}{2}$ and the ultraviolet scattering opacity of $\sim 0.5 \times 10^{-21}$ cm^2 at 1350 Å found by Perinotto & Patriarchi (1980a, b).

4.3.3. Ionizing Ultraviolet

For regions of large R, a radical change in the effective cross section between $\lambda \sim 1300$ Å and $\lambda \sim 912$ Å is not expected, and so the total opacity for ionizing radiation ($\lambda > 912$ Å) radiation is also approximated by equation (5). However, from the point of view of ionization the scattering component of the dust opacity is not very effective, for two reasons. First, the phase function in the ultraviolet is forward-throwing, so that absorption is most important in affecting the penetration. Second, if, as is discussed below, the gas covers a large solid angle about the Trapezium stars, then dust scattering simply redistributes the photons in direction and does not, to first order, diminish the total number of ionizations. Adopting an albedo of $\frac{1}{2}$, we find that the effective optical depth for ionizing photons is

$$\tau_g(912) = 0.5 \times 10^{-21} \int N_H dl \, . \qquad (6)$$

It is not possible for a source of relatively soft radiation, such as an O star, to photoionize an optical depth to dust much greater than unity at 912 Å. Therefore, a limit to the ionized hydrogen column density can be established if the optical depth is known, and vice versa.

4.3.4. Application Using the Emission Measure

Consider the emission measure of the main component. Castañeda (1988) finds that the intensity ratio of component A to component B is roughly 4:1 close to the Trapezium. Although our data do not actually overlap the Trapezium stars, but start 30″ to the west, we adopt this ratio. We find an emission measure of 1.87×10^{25} cm^{-5} there (~ 30″–40″, Tables 1 and 5), so that the emission measure of component A (the ionized material closest to the molecular cloud) is $\sim 1.5 \times 10^{25}$ cm^{-5}. The electron density at this innermost, most highly ionized portion of the nebula is $N_e \sim 10^4$ cm^{-3}, so that from equation (6) we have $\tau_g(912) \sim 0.75$. Thus our assumptions in deriving equation (6) lead to consistency with our expectation that $\tau_g(912) < 1$ for the ionized zone. This result also indicates that the extent of the ionized region might be dust-limited, by direct absorption of ionizing photons. The estimated optical depths for lines of sight passing farther from the star are generally somewhat smaller; these regions might be illuminated and/or seen obliquely. Note that an appreciable dust absorption optical depth between the star and the ionization front is a prerequisite for the dust to thermalize a significant fraction of the stellar luminosity, as is observed; the other inference is that optically thick clouds cover a good fraction of 4π steradians around the stars.

If the effective optical depth at ionizing wavelengths is less than unity, then it must be even less at optical wavelengths. For example, for the path corresponding to the main emission component in the inner brightest slit position, we predict $E(B-V) \sim 0.14$, so that the effective reddening for lines when dust is mixed with the emitting gas is probably less. We show below that any foreground emission component contributes even less. Comparison with both the reddening derived from the emission lines (0.34, Table 1) and the reddening of the Trapezium stars (0.28–0.36) implies that the reddening must arise in neutral material in front of the H II region, an important clue to the geometry.

4.4. The Line of Sight to the Trapezium

As a probe of a single line of sight through the H II region, emission lines are not without complications. For example, scattering not only dilutes the radiation emitted along a particular ray but also adds radiation from the other rays. Additionally, emission lines are sensitive to the square of the density, and not simply to the mass or column density of the matter involved. A special line of sight is present in the nebula, however, that to the source of ionizing radiation, θ^1 Ori C. Absorption by both the nebular gas and all intervening dust affects the spectrum of this star in a fairly simple way, because the radiation temperature of the star is so much greater than that of the nebula. Foreground gas is unambiguously detected by absorption measurements, revealing both ionized (metastable He I 2 ^3S state) and neutral (Ca II absorption, Lyα absorption, and the large reddening) gas. Note that this path through the foreground of the Orion complex is complementary to that studied in emission lines, since the main emission component arises between the star and the background molecular cloud.

4.4.1. The Neutral Component

Ca II absorption has three components, two of which are associated with extensive clouds in the foreground covering the

nebular complex (Adams 1944). A third at 4 km s^{-1} has the same velocity as the He I absorption line (see below), suggesting a spatial relationship. This component is not local to the θ^1 Ori C line of sight, being seen in three other stars. Since the ionization potential of Ca$^+$ is only 11.9 eV, this gas must be on this side of a foreground ionization front which is optically thick to ionizing radiation.

The reddening to θ^1 Ori C is $E(B-V) = 0.32$ mag (Bohlin & Savage 1981). The reddening varies smoothly over the nebula (Fig. 6) and is not peculiar only to his line of sight. Breger et al. (1981) find that typical foreground stars have smaller reddenings, $E(B-V) = 0.05$, so that most of the reddening to θ^1 Ori C [$E(B-V) = 0.27$; $A_V = 1.5$] must take place within the Orion complex. Since the observed reddening corresponds to a dust optical depth of $\tau_g(912) \sim 3$, most of the hydrogen associated with this dust must be neutral gas on this side of the foreground hydrogen ionization front.

The suggestion that hydrogen is largely neutral along the line of sight to the Trapezium is confirmed by *Copernicus* observations. From the Lyα absorption equivalent width Savage & Jenkins (1972) found a total neutral column density to the Trapezium cluster of $\int N_{H^0} dl \approx 1.1 \times 10^{21}$ cm^{-2}. This H^0 column density corresponds to a Lyman continuum optical depth of about 7000, showing that the gas is well shielded from ionizing radiation. The uncertainty in the H^0 column density deduced from the Lyα observations is large, but supports the contention that much of the extinction to the Trapezium stars occurs in the neutral region ($A_V \sim 0.6$ mag for this column density if eq. [4] is valid). We note below that the ionized column density might be much less.

4.4.2. The Ionized Component in Absorption

Line absorption from the metastable He I 2 ^3S state along the line of sight to θ^1 Ori C has been studied by Wilson (1937) and by Adams (1944). The observations of Adams complement ours (Fig. 3), since they are of much higher spectral resolution. He finds the He I line to be split into two components, with heliocentric velocities ~ 2–4 and ~ -30 km s^{-1}. Although Adams makes no quantitative measurements, his comments suggest that most of the equivalent width that we measured arises in the redward 2–4 km s^{-1} component, which we have seen is ionization-bounded. The strongly blueshifted He$^+$ component might either lie between θ^1 Ori C and the redward component, in which case it can be photoionized by the star, or be associated with the expanding shell discussed by Cowie, Songaila, & York (1979), in which case it must be ionized by other means. The blueshifted component must originate in a region of very low emission measure, since it is only weakly detected in the emission lines (Castañeda 1988). In the low-resolution *IUE* observations of Franco & Savage (1982), this blueshifted component might blend with the others.

We now use the He I 2 ^3S absorption to determine the H$^+$ column density. The curve of growth described above shows that the column density in He^0 2 ^3S is $\approx 8 \times 10^{13}$ cm^{-2}, with an uncertainty of roughly a factor of 2. The population of the 2 ^3S state is related to the total ionized helium abundance by the balance between radiative recombination, electron exchange collisions to the singlets, and radiative decays to ground (Osterbrock 1988). This balance is then (Clegg 1987)

$$\frac{N_{2\,^3S}}{N_{He^+}} = \frac{5.79 \times 10^{-6} t_4^{-1.18}}{1 + 3110 t_4^{-0.51} N_e^{-1}}, \qquad (7)$$

where $t_4 \equiv T_e/(10^4 \text{ K})$. Assuming $t_4 = 0.903$ and $N_{H^+} \approx 10$

N_{He^+}, and suppressing the dependence on filling factor, we find an H$^+$ column density of

$$\int N_{H^+} dl \approx 1.2 \times 10^{20}(1 + 3250 N_e^{-1}) \text{ cm}^{-2}, \qquad (8)$$

and a corresponding emission measure

$$\int N_{H^+} N_e dl \approx 1.2 \times 10^{20}(N_e + 3250) \text{ cm}^{-5}. \qquad (9)$$

These relations can be used to set limits to the density and size of the ionized gas along the line of sight to the Trapezium.

Using a different geometrical model to analyze the emission measure, Schiffer & Mathis (1974) concluded that the line-of-sight ionized column density was 3×10^{21} cm^{-2}. For a normal gas-to-dust ratio, there are two problems with a large column density of ionized gas. First, extinction in the ionizing ultraviolet would prevent the ionization of such a large column in the first place. By requiring $\tau_g(912) \leq 1$ for the H$^+$ zone along the line of sight, we find from equation (6) that $\int N_{H^+} dl \leq 2 \times 10^{21}$ cm^{-2}, probably less than that of the neutral component. Combining this with equation (8), we find the weak limit $N_e \geq 200$ cm^{-3}. A second problem with a large ionized column is that at optical wavelengths there could be too much reddening (recall that there is neutral gas too). With a low estimate it is not necessary to postulate a decreased dust-to-gas ratio in the ionized gas near the star (see § 4.5).

4.4.3. The Ionized Component in Emission

If the density in the ionized column were as low as 200 cm^{-3}, then the emission measure is $\sim 4 \times 10^{23}$ cm^{-5}, which is an order of magnitude less than that of Castañeda's (1988) component B emission. Component B has been interpreted as gas in the foreground of the flow, but whether it is in front of θ^1 Ori C is open to discussion. For example, component B (~ 8–14 km s^{-1}) does not have quite the same velocity as the above He$^+$ and Ca II components (4 km s^{-1}). If we were to assume that the component B emission measure of $\sim 4 \times 10^{24}$ cm^{-5} arises in the foreground ionized column, more stringent limits on the density would be obtained. This emission measure combined with the above limit on the column density from $\tau_g(912)$ implies $N_e > 2000$ cm^{-3}.

More interesting still is the combination of this emission measure with the prediction from He$^+$ in equation (9), which gives $N_e > 3 \times 10^4$ cm^{-3}. For the latter, from equation (8) we find an ionized column density through component B of order 1.3×10^{20} cm^{-2} (not too sensitive to the exact value of N_e), and now an order of magnitude less than the neutral column density. The amount of extinction associated with this ionized column would be negligible. The thickness of the ionized zone would be only of order $4 \times 10^{15}(3 \times 10^4/N_e \epsilon)$ cm.

Since both major foreground and background (component A) line-forming regions are optically thick to ionizing radiation, then, neglecting dust absorption of the ionizing radiation, the ratio of their emission measures is inversely proportional to the square of their distances from θ^1 Ori C (see also eq. [3]). Thus the distance from θ^1 Ori C to the foreground ionization front is at least twice, and perhaps 6 times, that to the main component at the molecular cloud, the wall of the blister. However, even this distance (0.2–0.6 pc) is small compared with the angular extent of the nebula. Therefore, θ^1 Ori C appears to lie between two relatively thin ionized sheets of considerable lateral extent.

4.5. Scattered Light and Polarization

Scattering properties of dust in the Orion Nebula have been studied by, among others, Simpson (1973), Schiffer & Mathis (1974), Perinotto & Patrarchi (1980a, b), and Mathis et al. (1981). The linear polarization has been imaged by Pallister et al. (1977). The arrangement of electric vectors normal to the radius vector from the Trapezium identifies the latter as the primary source of illumination. Similarly, the Trapezium is near the peak of the nearly circularly symmetric surface brightness distribution of the fluorescently excited 2–1 $S(11)$ H_2 line emission (Hippelein & Münch 1989).

White, Schiffer, & Mathis (1980) have considered the scattered light and polarization in the context of a hybrid geometrical model, in which dust is arranged both in a slab behind the star and in a hemisphere in front. Because of the (expected) forward-throwing phase function of the dust particles, the scattered flux is dominated by foreground material. However, the background slab can make a significant contribution to the polarized flux at small offsets of 1′–2′. The degree of polarization has not been interpreted in detail because there is a large correction for (low-polarization) gaseous emission in the B filter. However, from the uniformity of the degree of polarization with azimuth they conclude that the normal to the slab component cannot be significantly tilted to the line of sight (more generally, the line of sight is close to an axis of symmetry of the geometry). This symmetry is not so clear from comparison of the radio continuum surface brightness (the ionized component) with molecular maps, such as of CS (Osahi et al. 1989).

In the scattering models described by Mathis, Schiffer, and coworkers there is a "hole" of angular size $\sim 2′$–$3′$ (0.29–0.43 pc) in the radial density distribution of dust, in order to fit the optical surface brightness profile as a function of distance from the Trapezium. It was envisioned that the dust is mixed with the ionized gas, and because the gas in their adopted model peaks in density toward the center, it was concluded that the dust-to-gas ratio had to be lower close to the Trapezium. We do not feel that a lower dust-to-gas ratio is needed: while a low density of dust close to the Trapezium appears to be required (by "close" we refer here to the displacement in three dimensions, rather than the apparent offset or impact parameter), the hypothesized high gas density close to the Trapezium is not required. In fact, according to our analysis of the emission-line components and the line of sight to the Trapezium, there could be a dearth of ionized gas close to and in front of the Trapezium, and so nothing unusual is required of the dust-to-gas ratio in the ionized gas. In our picture the optical depth of the foreground material is significant (1.5–2 at $H\beta$); but, as discussed above, the gas associated with this large a dust column cannot be ionized, and instead our analysis pointed to the foreground dust being associated with neutral gas. The dust-to-gas ratio in the ionized gas cannot be deduced separately.

A region of relatively low gas and dust density around a massive luminous star is not unexpected, because of the effects of radiation pressure and a stellar wind (Pankonin et al. 1979). High-velocity (150 km s^{-1}) material is seen near θ^1 Ori C (within 10″), indicating flows that could clear out the surrounding medium (Meaburn 1988). Radio continuum maps (Barvainis & Wootten 1987) show a central depression in surface brightness of diameter 15″, which is smaller than the hypothesized dust hole. We interpret this observed depression as a cavity formed in the high surface brightness background ionized zone. However, the larger dust hole is required only in

the foreground. In the direction toward us, away from the dense molecular cloud in the direction of the champagne flow, it seems reasonable that a hole of somewhat larger extent could have been excavated.

Scattering of the stellar continuum by dust in the nebula can be seen by the elevated level of continuum emission in Figure 2. Close to the star our data are in agreement with earlier measurements. Other data at lower spatial resolution and along different radial directions from the Trapezium show a major increase in the continuum-to-line ratio for offsets of 3′–5′ (see summary in Schiffer & Mathis 1974). Our measurements show a similar, but weaker, gradient for the direction west of θ^1 Ori C. In the picture being developed here, the emission lines are produced largely in the background ionized material at the surface of the molecular cloud, whereas the scattered light could be primarily from dust associated with unrelated foreground neutral gas.

5. PHOTOIONIZATION CALCULATIONS

Among our main goals is a determination of the gas phase abundances in the H II region. In the particular case of helium we need to determine whether a correction must be applied for the presence of atomic helium in the ionized hydrogen zone (Osterbrock 1988), whether the hydrogen lines have their case B emissivity (Cota & Ferland 1988), and the collisional contribution to the helium lines. Since these corrections introduce systematic errors, they are pivotal; they can best be made by consulting results of a realistic simulation of the physical conditions in the nebula. In turn, the merits of the simulation can be judged by a detailed comparison with a variety of observations.

5.1. A Mean Emission-Line Spectrum

In this section we derive a mean spectrum for the innermost regions of the nebula, $\approx 40″$ west of θ^1 Ori C, where the nebula is brightest and the spectrum is best observed. Reproducing the spectrum of this region will be the object of the photoionization calculations presented below.

The mean, reddening-corrected spectrum is summarized in Table 7, all strengths being with respect to $H\beta$. For the optical data presented in this paper, we averaged reddening-corrected intensities over the two innermost slit positions. As a result we can assign an uncertainty to each intensity, based on both measuring errors and the observed change in the spectrum with position. The indicated uncertainty is the greater of the scatter between the two slit positions and 5%. Systematic errors are also present, but should be of order 10% or less.

Besides the optical line intensities, we also consider ultraviolet and infrared line observations. Intensities taken from the literature are indicated by a colon beside the entry, together with a reference to the original paper. Cospatial measurements were not available, but, where possible, line intensities were taken from regions roughly 40″ from θ^1 Ori C, at any position angle. Because both the intrinsic emission-line spectrum and reddening change with position in the nebula, these supplementary measurements provide only a rough estimate of the strengths these lines would have at our position 40″ west of θ^1 Ori C. However, even allowing for a factor of 2–3 uncertainty, these extra lines still help to constrain the model and place very much tighter limits on the size of any possible correction for neutral helium.

Table 8 lists quantities important for determining the parameters of the model (§ 5.4). The reddening-corrected

TABLE 7

EMISSION-LINE STRENGTHS RELATIVE TO Hβ

Line (1)	Species (2)	I(line)$_{corr}$[a] (3)	I(line)$_{calc}$ (4)
λ3727	[O II]	0.94 ± 0.20	1.18
λ3869	[Ne III]	0.20 ± 0.03	0.209
λ4340	Hγ	0.49 ± 0.03	0.510
λ4363	[O III]	0.015 ± 0.003	0.014
λ4471	He I	0.046 ± 0.003	0.043
λ4861	Hβ	1.000	1.000
λ5007	[O III]	3.43 ± 0.17	3.510
λ5577	[O I]	0.002 ± 0.001	...
λ5755	[N II]	0.0104 ± 0.0005	0.0070
λ5876	He I	0.137 ± 0.007	0.133
λ6300[h]	[O I]	0.007:	0.003
λ6563	Hα	2.77 ± 0.14	2.705
λ6584	[N II]	0.442 ± 0.088	0.401
λ6678	He I	0.036 ± 0.002	0.036
λ6725	[S II]	0.051 ± 0.003	0.0503
λ7135	[Ar III]	0.154 ± 0.008	0.153
λ7325	[O II]	0.119 ± 0.006	0.132
λ9532	[S III]	1.445 ± 0.285	1.95
λ1909[b]	C III]	0.18:	0.248
λ2326[b]	C II]	0.14:	0.082
λ2798[c]	Mg II	<0.012:	0.010
λ4658[g]	[Fe III]	0.008:	0.008
52 μm[d]	[O III]	0.25:	0.301
88 μm[d]	[O III]	0.036:	0.040
57 μm[d]	[N III]	0.031:	0.054
36 μm[d]	[Ne III]	0.040:	0.049
158 μm[f]	[C II]	0.07:	0.0003
63 μm[f]	[O I]	0.2:	0.0002
λ10830[e]	He I	0.8:	0.423
λ7291[e]	[Ca II]	<0.0006	0.0006

[a] Line intensities relative to Hβ corrected for reddening and for underlying absorption in the scattered starlight, and averaged over the two innermost slit positions. Indicated uncertainties are the larger of the standard deviation between the two, or 5% of the measured quantity, except that 20% error bars are used for λ4363 and λ6548 because of blending problems. A colon indicates intensities measured elsewhere in the nebula.

[b] Torres-Peimbert, Peimbert, & Daltabuit 1980.

[c] Perinotto & Patriarchi 1980.

[d] Simpson et al. 1986; see also Rubin et al. 1988.

[e] Osterbrock, Shaw, & Veilleux 1990.

[f] Tielens & Hollenbach 1985a.

[g] Kaler 1976.

[h] Peimbert & Torres-Peimbert 1977.

TABLE 8

CONSTRAINTS ON MODEL PARAMETERS

Quantity (1)	Observed (2)	Predicted (3)
F(Hβ)[a]	4.9	4.81
λ5007/λ4364	229 ± 34	251
λ6584/λ5755	42.5 ± 6	57.2
λ6731/λ6717	1.81 ± 0.09	1.94
λ3727/λ7325	7.90 ± 1.85	8.98
$T_{graphite}$ (K)	∼100	145
$T_{silicate}$ (K)	∼100	116
I(Hβ)/I(case B)	...	0.9786
IR/I(Hβ)[b]	...	134.2

[a] Observed F(Hβ) in units of 10^{-12} ergs cm^{-2} s^{-1} arcsec^{-2}; reduced by $\frac{4}{5}$ to correspond to line component A, which is modeled.

[b] Integrated intensity of grain thermal emission, relative to Hβ.

surface brightness of Hβ is a factor $\frac{4}{5}$ of the total, since we intend to model component A.

5.2. Geometrical Considerations

As discussed above in § 4.1, kinematic data (Castañeda 1988) show that most of the observed emission originates in the component nearer the molecular cloud. The relative emission measure of the blueshifted and redshifted components suggests that the star is closer to the molecular cloud ionization front than to the neutral cloud along the line of sight (§ 4.4). In the following we concentrate on modeling the emission from the brighter, background component. Ionizing radiation creates an ionization front, through which gas flows from the cold molecular cloud into the hot ionized regions. The flow is expected to occur at nearly the gas sound speed, and at nearly constant pressure. In our models we assume that the emission-line region is time-steady and has constant gas pressure. In computing the line widths, a microturbulence of 8 km s^{-1} is adopted, as suggested by very high resolution line observations (Castañeda 1988).

Two limiting cases can be identified for the geometry and its effects on the emission-line spectrum (Van Blerkom & Hummer 1967): an open geometry in which gas covers a small fraction of 4π sr as seen from the central star, and a closed geometry in which gas fully covers the central star. The main effect is on diffuse ionizing photons produced at the illuminated face of the cloud by recombinations to the ground state of H and He. In an open geometry, roughly 50% of these diffuse ionizing photons escape from the system, and the effective recombination coefficient for hydrogen or helium at the face of the cloud is midway between the case A and case B limits. By contrast, in a closed geometry the diffuse ionizing photons which escape from one side of the nebula go on to strike the other side, causing ionizations there. If the geometry is closed and symmetric, then the "on-the-spot" approximation is an excellent assumption (Van Blerkom & Hummer 1967; Bässgen, Bässgen, & Grewing 1988). Evidence summarized above indicates that radiation-bounded clouds nearly fully cover the Trapezium stars, and so it seems that a closed geometry is the best assumption. Our model is therefore basically a plane-parallel slab of constant gas pressure located some distance away from the source of ionizing radiation, θ^1 Ori C.

In general, we must also consider scattering processes (i.e., Rayleigh, electron, and dust scattering). In a closed geometry scattering does not diminish the total number of ionizing photons available, since scattered photons go on to interact elsewhere in the system; the effect on the ionizing continuum locally in the nebula is minimized when the system is symmetric. Scattering in a medium which is also absorbing affects the details of where in the nebula the ionizing photons interact. In the present situation the scattering opacity is dominated by dust which has a strongly forward-throwing phase function; this greatly diminishes the effect of scattering on the penetration of ionizing photons into the nebula. For these reasons, we neglect scattering in treating the attenuation of the incident radiation field.

5.3. Physical Processes Involving Grains

There is evidence that the presence of grains within the H II region cannot be neglected in models of the emission-line regions. For instance, the largest observed emission measure and the inferred H$^+$ column density suggest that the column

density of embedded dust is large enough to result in a significant dust optical depth at ionizing energies (§ 4.3). Also, infrared data show that the thermal emission from warm grains near the Ney-Allen Nebula is strong, again suggesting that the grains are effective at absorbing ionizing radiation from the central stars. Appendix C describes the changes made to version 76 of the photoionization equilibrium code Cloudy, last described by Ferland (1990), to incorporate some physical processes relating to grains, as well as some other details.

5.4. *Model Calculations*

We model the component of the H II region identified as the flow moving toward us, away from the molecular cloud. We assume constant gas pressure, steady state, and that the grain opacity shown in Figure 19 does not vary with depth. Appendix C gives further details on our numerical procedures.

A photoionization calculation must make assumptions concerning the geometry, e.g., the angle at which we view the H II region with respect to the beam of ionizing radiation. We assume that the flow is plane-parallel. Since such a model is well defined, its surface brightness is a straightforward parameter, and it is hard to see how we can do much better. The fact that the main flow occurs at a distinct velocity component does suggest that the wall of the blister is well defined. Following the discussion in § 4, we assume perpendicular illumination and perpendicular viewing; deviations from this geometry would become more significant at large offsets from θ^1 Ori C.

5.4.1. *Parameter Selection*

Given our assumptions, the free parameters are (a) the flux of ionizing photons at the illuminated face of the flow (this is equivalent to specifying both the luminosity and distance of the star), (b) the density of the flow at the illuminated edge, (c) the composition of the gas, and (d) the temperature of the star. These are varied to match the reddening-corrected spectrum as closely as possible. The actual choices for the free parameters are summarized in Tables 9 and 11, and are discussed below.

The flux of ionizing photons was adjusted in order to reproduce the observed dereddened surface brightness in the hydrogen lines, 4.9 ergs s^{-1} cm^{-2} arcsec^{-2} at Hβ (the fraction of the total observed emission which is likely to originate in component A). If the total number of ionizing photons emitted by θ^1 Ori C is characteristic of an O6 star [$Q(H) \sim 10^{49}$ s^{-1}; Osterbrock 1988], then the inferred flux, $\phi(H) = 10^{13}$ cm^{-2} s^{-1}, corresponds to a star-flow separation of $\sim 3 \times 10^{17} Q_{49}^{1/2}$ cm. This distance is comparable to the projected slit distance (Table 5), confirming that θ^1 Ori C is indeed quite close to the wall of the blister.

The hydrogen density at the illuminated face was adjusted to match simultaneously the [S II] doublet ratio, the [N II] $\lambda5755/$ $\lambda6584$ ratio, and the [O II] $\lambda3727/\lambda7325$ ratio. Constant gas

pressure was assumed to relate the density deeper within the flow to that at the surface. The deduced hydrogen nucleon density at the inner face is $10^{4.0}$ cm^{-3}. The deduced ionization parameter is log $U = -1.48$. The global composition of the gas was varied to reproduce the electron temperature deduced from the observed [O III] $\lambda4363/\lambda5007$ intensity ratio. The gas phase abundances of individual elements were varied to reproduce the observed intensities of individual lines, as discussed below.

Newly recomputed Kurucz line-blanketed LTE atmospheres (Kurucz 1979, 1989) were used for the incident stellar continuum; the surface gravity was log $g = 4.5$, and solar abundances were assumed. Interpolation on the grid of atmospheres was performed by linear interpolation in log T_{eff}–log F_ν space. The temperature of θ^1 Ori C was varied to reproduce the strength of the forbidden lines relative to Hβ (Stoy 1933; Kaler 1978), the deduced value being 39,600 K.

The predicted emission-line strengths and line ratios are given in Tables 7 and 8 for comparison with the mean spectrum.

5.4.2. *Physical Conditions*

Some physical properties of the model as a function of position are shown in Figure 16. Panel *a* gives the electron temperature and total hydrogen density. The gradual increase in temperature within the H$^+$ zone is caused by the interplay between the gas heating rate, which tends to increase with depth due to the hardening of the transmitted radiation field, and the gas cooling rate, which depends on the variety of ions present. There is a rapid fall in the temperature at the H^0–H$^+$ ionization front, and because the pressure is constant and nearly proportional to the product $T_e N_H$, the density rises to compensate. The oxygen ionization structure shown in panel *b* is typical of the heavy elements.

As originally suggested by Maciel & Pottasch (1982) and Oliveira & Maciel (1986), photoelectric heating of the gas by grain photoionization is an important heating mechanism in the H II region, and produces significant changes in the global energy budget of the nebula. Panel *c* shows the fraction of the total gas heating/cooling due to grain photoionization. The local heating of the nebula is most affected in the inner most highly ionized regions, where grains provide the dominant opacity at ionizing energies, and in the outer regions in the H^0–C$^+$ zone, where only the Balmer continuum is present, since the Lyman continuum has been heavily attenuated, and again grains are the main absorber. The fraction of the total cooling due to gas collisions with grains is also shown. This depends mainly on the electron kinetic temperature, and so varies less than the heating. The ratio of grain heating to cooling mainly depends on the ratio of the mean photoelectron energy to the electron kinetic energy. This ratio decreases deep in the nebula, where Balmer continuum photons are the main ionization source of the grains, with the result that a typical photoelectron energy is small. Grains contributed 12% of the total photoelectric heat input in the model, and produced as much as 34% of the heating in the outer transition zone. Globally, the grain cooling contributed 4.7% of the total cooling and reached as much as 27.5% of the cooling in certain regions.

The grain temperature was typically $\sim$100–150 K across the H$^+$ zone, as shown in panel *d*. Direct absorption of the incident continuum was the major grain heating mechanism, amounting to $\approx$83% of the total dust heating (Lyα contributed

TABLE 9
MODEL PARAMETERS

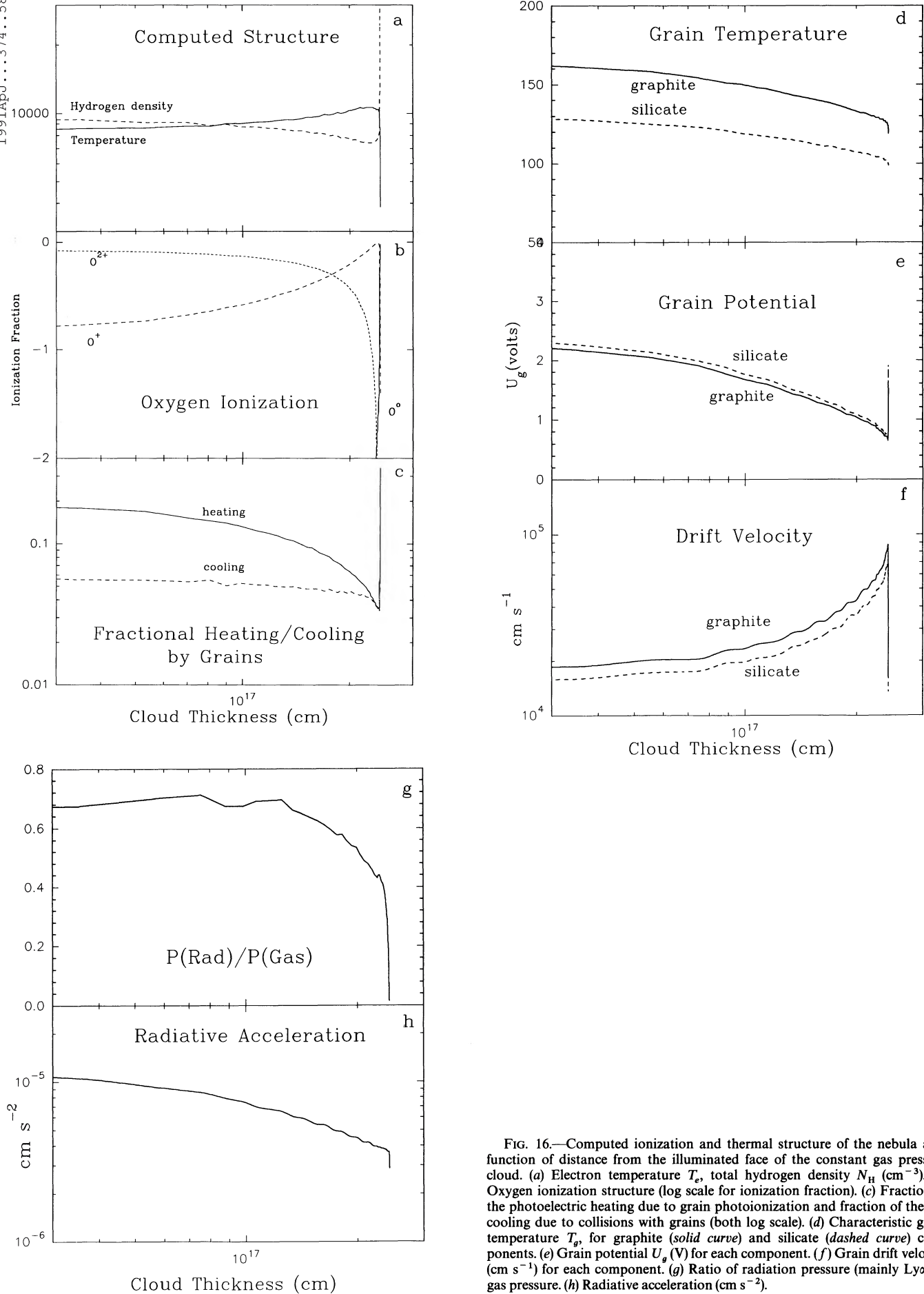| Quantity (1)	Value (2)
T_{star}	39,600 K
$\phi(H)$	10^{13} cm^{-2} s^{-1}
log g	4.5
N_H(inner)	10^4 cm^{-3}
P_{gas}	2.35 × 10^{-8} dynes cm^{-2}
V_{turb}	8 km s^{-1}

FIG. 16.—Computed ionization and thermal structure of the nebula as a function of distance from the illuminated face of the constant gas pressure cloud. (a) Electron temperature T_e, total hydrogen density N_H (cm^{-3}). (b) Oxygen ionization structure (log scale for ionization fraction). (c) Fraction of the photoelectric heating due to grain photoionization and fraction of the gas cooling due to collisions with grains (both log scale). (d) Characteristic grain temperature T_g, for graphite (solid curve) and silicate (dashed curve) components. (e) Grain potential U_g (V) for each component. (f) Grain drift velocity (cm s^{-1}) for each component. (g) Ratio of radiation pressure (mainly Lyα) to gas pressure. (h) Radiative acceleration (cm s^{-2}).

much of the remainder). The temperature therefore decreases with depth as the incident ionizing radiation field is attenuated. The maximum grain temperature achieved depends on the flux of ionizing photons, which has been fixed by matching the observed emission measure.

The total extinction $E(B-V)$ through the H^+ zone of our model is ~ 0.2 mag. This suggests that the increased reddening observed at small offsets from θ^1 Ori C is caused by internal extinction within the H II region. This effect also accounts for the differential extinction observed by Greve et al. (1989) between hydrogen lines (formed near the midpoint of the H^+ zone) and [S II] lines (formed near the H^0–H^+ ionization front).

The grain potential U_g was typically between 1 and 2 V, as is shown in panel e. The change in the potential is the result of the interplay between the intensity of the radiation field, which tends to increase the potential, and the positive potential itself, which lowers the effective photoelectric yield (see Appendix C). The grain drift velocity is shown in panel f. The behavior with depth results from the interplay between the intensity of the incident radiation field, which not only pushes the grains but also ionizes them to increase their drag, and the ionization of the gas, which provides the Coulomb drag force.

Panels g and h of Figure 16 show two quantities related to the dynamics of the nebula (a static geometry was assumed in the calculation, however). The upper panel shows the ratio of radiation to gas pressure. This was computed as in Elitzur & Ferland (1986), the major contributor to the radiation pressure being Lyα. The gas pressure was held constant across our calculation rather than the total pressure, because the deduced geometry is not stable; a plasma dominated by radiation pressure can be stable only if it is self-gravitating. This may account for the observation that high-ionization lines in Orion are blueshifted relative to the low-ionization lines.

5.4.3. Infrared Continuum Emission

The Orion complex is a strong source of thermal emission from dust. Maps in the 10 μm spectral band (Gehrz, Hackwell, & Smith 1975) reveal two main regions, heated by the Trapezium (the Ney-Allen Nebula; Ney & Allen 1969) and by the infrared cluster in OMC-1 (the Kleinmann-Low Nebula). Maps at 20, 50, and 100 μm (Werner et al. 1976) show the latter becoming predominant at longer wavelengths. In fact the cooler KL component becomes so strong that it becomes difficult to extract the contribution of grains heated by the Trapezium (see the maps, or the mid-infrared spectrum in Forrest, Houck, & Reed 1976).

Some data are compared with the predicted surface brightness of our model in Figure 17. We have adopted the 3.4–18 μm data from Ney, Strecker, & Gehrz (1973), choosing as representative the measurements centered on θ^1 Ori C with a 25" aperture (60" chop); at 3.4 and 4.7 μm we made an approximate subtraction of the stellar component using their multi-aperture data. This gives a surface brightness spectrum similar to that at the Ney-Allen peak, but a factor of 0.4 lower. The 50 and 100 μm points are estimated with considerable uncertainty from the contour maps of Werner et al. (1976). The agreement with the model, which has a full complement of dust mixed with the gas, is remarkably good. Our model underestimates the surface brightness particularly at 3.4 μm. This could be due to the emission features of PAH arising near the photo-dissociation region adjacent to the ionization front (Allamandola, Tielens, & Barker 1989), which we have not modeled; it is not a large factor in the overall energy budget.
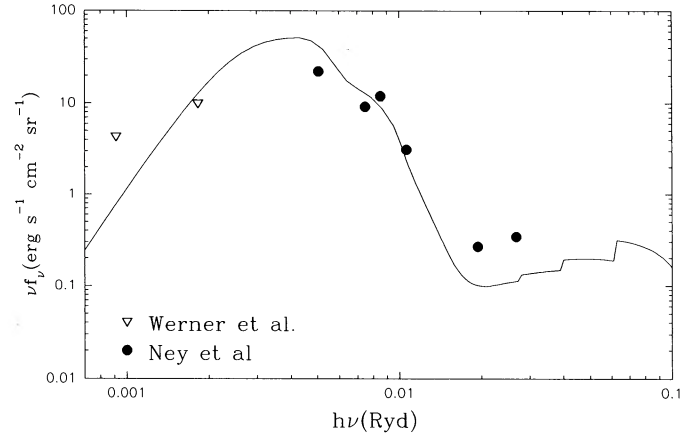

FIG. 17.—Predicted cloud surface brightness, including gas and dust emission. Observed points are from Ney et al. (1973) and Werner et al. (1976). The lowest energy point is contaminated by emission from OMC-1.

Neglect of the foreground dust should be unimportant at 10 μm, since the material is further from θ^1 Ori C than is the background slab. Note that the calculation is for the region 40" *west* of θ^1 Ori C, near the position of peak emission measure, while the infrared surface brightness peaks to the *east* of θ^1 Ori C near θ^1 Ori D. The peak near θ^1 Ori D would be interpreted as localized hotter dust close to that star. For more detailed agreement with the observations near 10 μm (which are centered on θ^1 Ori C), our model would have to have some somewhat hotter silicate grains. We have made the approximation of a single grain temperature for all sizes, whereas in actuality the smaller grains within the distribution will be hotter; their effect would be most noticeable on the Wien tail of the Planck function.

In a nebula in which the main source of grain heating was diffuse Lyα radiation the grain temperature as a function of distance from the star would be fairly constant. However, the observed lack of a strong color gradient in the central regions does not necessarily imply Lyα heating. Instead, it is probably related to geometry. Our model is of a background slab with no dust (or gas) close to the central star, where it could be an order of magnitude hotter than observed; this is to be contrasted with a filled spherical model which would have a strong temperature gradient away from the star. In our model direct absorption of continuum radiation is in fact a much larger source of grain heating than Lyα.

5.4.4. The Emission-Line Spectrum

Although the model is largely successful (see Tables 7 and 8), it does underpredict the intensity of some [O I] and [C II] lines. The infrared fine-structure lines are expected to be formed in the relatively cool photodissociation region (Tielens & Hollenbach 1985a, b), which our photoionization model, like others does not yet attempt to model. It seems posssible that some [O I] λ6300 is produced in the intermediate warmer region near the H^+–H^0 ionization front (Burton, Hollenbach, & Tielens 1990).

Dust absorption does affect the intensities of certain lines because of resonance scattering. Virtually all Lyα is destroyed by absorption on grains. The intensity of the He I λ10830 line is also affected, being reduced to roughly half the intensity found in a dust-free gas. This is largely the result of the increased path length caused by resonance scattering (the optical depth is ~ 600; see also Clegg & Harrington 1989). The He I λ3889 line is similarly weakened. The He I lines used in our analysis do

not arise from metastable levels, and are predicted to be optically thin. As a result, their transport out of the line-forming region should be no different from the hydrogen Balmer or Paschen lines. We have chosen to deredden the observations of these lines for comparison with our model, instead of accounting for the reddening in the model predictions; this allows effectively for both internal and foreground dust.

The predicted hydrogen and helium lines in Table 7 are the result of self-consistent calculations of the level populations (see Ferland & Rees 1988 for a discussion of the treatment of hydrogen). In agreement with what was inferred above from the observations, the $H\alpha/H\beta$ ratio is predicted to be slightly below case B. Collisional excitation of helium is predicted to enhance the emissivity of some lines; for instance, $\lambda5876$ is increased by 10% over its case B prediction. This is despite the importance of Lyα photoionization of the 2 ^3S level, which diminished the level population $\sim23\%$ below that expected from collisions alone (eq. [7]).

5.4.5. The Helium Abundance

We now investigate what corrections to the ionic abundances must be made to derive a helium abundance, and whether the Balmer lines are expected to have case B emissivity, which was assumed. Mean ionization fractions for the 13 elements included in the calculation, averaged over radius, are listed in Table 10. The calculation shows that the He$^+$ and H$^+$ zones are nearly coextensive, so that the correction for neutral helium in the ionized hydrogen zone amounts only to $+3.2\%$, in the sense of increasing the helium abundance. In fact, for a (dust-free) nebula ionized by such a hot star, only a small correction for neutral helium is expected (Osterbrock 1988). Aannestad (1989) has shown how selective extinction of ionizing photons by nebular dust (Fig. 19a) tends to increase the level of ionization and in particular to merge the He$^+$ and H$^+$ boundaries even for somewhat cooler stars.

Note that the Ne abundance derived (Table 11) is higher than solar; this is based on the [Ne III] $\lambda3869$ line which arises from Ne^{++}, not the dominant stage of ionization (Table 10). This probably signals that the flux of the Kurucz atmosphere at energies in the otherwise poorly constrained range above 40 eV is low; this extra hard radiation (which we have not modeled) would reduce the above correction for neutral He.

The correction for the deviation from case B caused by dust destruction of hydrogen Lyman lines was calculated as in Cota & Ferland (1988). This amounts to only a -2.2% effect, nearly

canceling the above correction for neutral helium. Continuum fluorescence induced by the continuum of the star is another small effect; this increased the intensity of $H\beta$ by $+0.4\%$. The total result of these considerations is that the helium abundance is essentially unchanged: $He/H = He^+/H^+ = 0.088 \pm 0.006$. This low-ionization correction factor is entirely consistent with Figure 12, which shows that the He$^+$/H$^+$ ratio indicated by the $\lambda4471/H\gamma$ ratio does not change despite large changes in the S^{++}/S$^+$ and O^{++}/O$^+$ ratios (see Figs. 10 and 11).

In principle, a further correction enters because the emission we observe originates both in the main flow from the molecular cloud, which we model, and in component B (roughly 20% of the emission in the [O III] line), which is possibly the ionized skin of the predominantly neutral sheet along the line of sight (the latter contributes much of the reddening; see above). If helium were predominantly neutral in the H$^+$ zone of this component, then a significant correction to the final helium abundance would be needed. Fortunately, the spectroscopic evidence suggests that the gas associated with the H$^+$ zone of this second component is highly ionized; the component is detected in [O III] emission, which is formed in the He$^+$ zone; and the line of sight to θ^1 Ori C has absorption due to metastable 2 ^3S (produced by He$^+$). Both suggest that helium would be well ionized in this second region, although it is not possible to quantify this with existing data (the line deconvolution into kinematic components has not been done for hydrogen or helium lines or for the [O II] lines). Despite evidence that the ratio of component A to component B intensities changes from position to position in the nebula (Castañeda 1988), the ionic helium abundance does not change with slit position in our data, and agrees with radio (and optical) data obtained at still other positions, again suggesting that the contribution from the second component has not distorted the ionic ratio.

5.4.6. Abundances and Depletion

The abundances of the other elements in the model are summarized in Table 11. These have been obtained by varying the individual abundances to match line strengths of that element. For comparison, depletions relative to solar values are listed. For the case of silicon, we assume a depletion of 0.16, suggested by infrared observations (Haas, Hollenbach, & Erickson 1986).

The table also gives a quality indicator, which is our subjective appraisal of the reliability of the individual abundances. The helium abundance has the greatest reliability, since it

TABLE 10

IONIZATION FRACTIONS[a]

	IONIZATION STAGE			
ELEMENT	1	2	3	4
H	0.0036528	0.9963472	...	...
He	0.0358712	0.9641288	0.0000000	...
C	0.0000207	0.1319186	0.8680106	0.0000501
N	0.0007813	0.1325985	0.8665633	0.0000570
O	0.0034633	0.4266920	0.5698447	0.0000000
Ne	0.0035733	0.9096719	0.0867548	0.0000000
Mg	0.0001329	0.0503695	0.9494976	0.0000000
Al	0.0000150	0.1011535	0.6785844	0.2202471
Si	0.0000039	0.0548831	0.8291673	0.1159360
S	0.0000012	0.0303454	0.9497464	0.0199070
Ar	0.0016812	0.1051803	0.8918426	0.0012960
Ca	0.0006767	0.0287490	0.9705671	0.0000072
Fe	0.0000579	0.0127783	0.2436043	0.7435595

[a] Averaged over radius.

TABLE 11

MODEL GAS PHASE COMPOSITION

Element (1)	Abundance[a] ($\times 10^4$) (2)	[Abundance][b] (3)	Quality (4)
He	...	0.90	A
C	2.12	0.59	D
N	0.87	0.77	C
O	3.81	0.44	B
Ne	3.95	3.19	D
Mg	0.032	0.08	D
Si[c]	...	...	...
S	0.133	0.72	B
Ar	0.021	0.58	B
Ca	0.0002	0.012	D
Fe	0.042	0.13	D

[a] Abundance by number relative to hydrogen.
[b] Abundance relative to solar (using Grevesse & Anders 1989).
[c] Depleted abundance assumed, since no lines available.

comes from a ratio of recombination lines, and our observations were designed with this atom in mind. A quality of B is assigned to the heavy elements in which we observed more than one ionization stage, or in which we have extensive data for the dominant stage of ionization. A quality of C indicates a somewhat greater uncertainty, since the dominant ionization stage is not observed with our data. D indicates those abundances which entirely rely on supplemental data, which are not cospatial with ours, and also applies to Ne, as described above.

Several elements, especially Mg, Fe, and Ca, appear to be very strongly depleted, probably in dust. Like previous nebular studies, we find the unusual result that O is underabundant relative to the solar value. The N/O ratio based on the optical lines is comparable to the value of 0.2 from the [N III] and [O III] infrared fine-structure lines (Rubin et al. 1988), as opposed to lower in earlier interpretations. Note that [N III] is potentially a better indicator than [N II], since it is dominant ion (Table 10).

6. DISCUSSION

6.1. *Primordial Helium and the dY/dZ Relation*

We find a helium abundance for the H II region of $He/H = 0.088 \pm 0.006$. This is $\sim 12\%$ lower than $He/H = 0.100$ (Peimbert et al. 1988), which is commonly quoted. A major difference between the two numbers lies with the correction for neutral helium used to convert the observed ionic abundance ratio into an abundance. The correction for neutral helium used by Peimbert and Torres-Peimbert (1977) and used in later papers was based on an empirical relation of He^+/H^+ and the [O II]/[O III] spectrum. The photoionization calculations presented here show that the correction for neutral helium should be small, and reproduce the [O II]/[O III] spectrum quite well. Our calculations also derive the gas phase abundances of the heavy elements (Table 11), several of which are strongly depleted. Assuming the gas phase abundances of Table 11, except solar for Ne, and adding the heavy elements present in the dust particles, our value of the metallicity Z is 0.011, with an estimated uncertainty of 20%, and Y is 0.257 ± 0.015.

In Figure 18 we show our Orion Nebula abundances in the context of the dY/dZ relation. The primordial solar abundances are from the summary of solar models by Turck-Chièze et al. (1988). At $Z = 0.005$ we show Y estimated from models of the horizontal-branch morphology in 47 Tuc (Dorman, VandenBerg, & Laskarides 1989). The other three low metallicity points are each averages of data for 12 blue compact galaxies, based on Table 2 of Olive (1990) and $Z = 25O/H$; they faithfully reproduce the fits given in his equations (3.2) and (3.3). Finally, we plot the value of Y_p from models of primordial nucleosynthesis, with the latest restrictions on η from light elements and on the neutron half-life (Olive 1990).

There appears to be a trend of Y increasing with Z. Indeed, all of the data are consistent with a single straight line, which from a weighted fit to the data is

$$Y = 0.240 \pm 0.002 + (1.52 \pm 0.38)Z . \qquad (10)$$

While this is provocative, it is not at all obvious that there should be a single relationship between Y and Z over such a range in conditions, since the chemical evolution in a galaxy depends on the stellar mass function. The intercept implied by all the observational data is $Y_0 = 0.238 \pm 0.004$ (slope 1.72 ± 0.54). Pagel (1989) has preferred to use only the blue compact galaxies, which from Figure 18 obviously give a
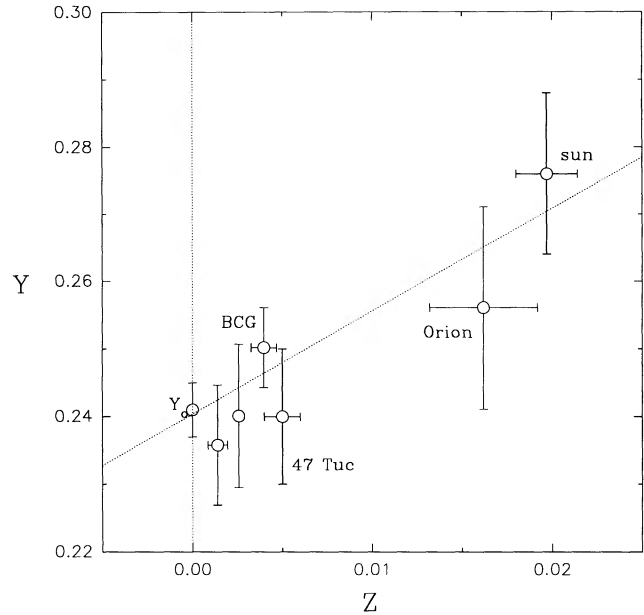

Fig. 18.—Current status of the dY/dZ relation. The value for Orion is from this work. The solar value is from Turck-Chièze et al. (1988). The point for 47 Tuc is from Dorman et al. (1989), and the points for blue compact galaxies (BCG) and the primordial helium abundance are based on the review by Olive (1990).

steeper slope and a smaller Y_0; the latter seems more at odds with constraints from standard big bang primordial nucleosynthesis (e.g., Krauss & Romanelli 1990 suggest $Y_0 > 0.235$).

6.2. *Summary*

Our main conclusions can be summarized as follows:

1. Several simple relations between offset and the surface brightness, density and ionization of the Orion Nebula are present along a 5' line west of θ^1 Ori C.

2. These support a very simple (and plausible) geometrical model in which θ^1 Ori C is sandwiched between two layers of ionized gas. The majority of the Hβ flux comes from a layer behind θ^1 Ori C, which represents gas boiling off the dense molecular cloud upon which the Orion Nebula is a blister.

3. Along this same line the ionic helium abundance is constant, with a mean value consistent with previous optical and radio observations. This suggests that helium is nearly fully ionized.

4. The uncertainties in the line ratios, and their conversion into ionic abundances, are dominated by systematic errors which we do not model. In particular, it seems likely that the hydrogen lines do not emit at case B, and that the Orion extinction law is not known to sufficient accuracy to allow a really precise determination of the helium abundance.

5. Photoionization models of the innermost regions of the nebula are computed to deduce the gas phase abundances. These explicitly include the effects of grains on the thermal balance of the nebula, and model the H II region as a flow from the distant molecular cloud. Photoelectric heating of the gas by grain photoionization, and cooling by gas-grain collisions, are important heating-cooling mechanisms in the H II region which change the global energy budget of the nebula. Radiation pressure is significant across the region we model.

6. Several heavy elements are depleted in grains in the H II region, as they are in molecular and diffuse clouds. The observations are consistent with dust being well mixed with gas, and

that a dust hole near the central star is accompanied by a minimum in the gas too.

7. Our calculations have been compared with the infrared emission from the "Ney-Allen" Nebula, the warm dust near the Trapezium stars. Our model is not sufficiently spatially inhomogeneous to account for the peaked emission near θ^1 Ori D, but does give the right order of magnitude for the surface brightness. The presence of these warm grains shows that dust is well mixed with gas throughout the nebula (see also Münch & Persson 1971). This calculation also verifies that our treatment of the grain energetics is consistent with the global energy budget of the H II region.

8. Our models, which give a very accurate fit to a wide variety of observed properties of the nebula, predict that the correction for neutral helium should be very small. This is in contrast to previous work, and leads us to deduce a He/H abundance ratio which is about 12% smaller than previous results.

9. The abundances we derive are consistent with a single dY/dZ relation spanning the range from primordial to solar abundances.

APPENDIX A

RADIO RECOMBINATION LINES

Radio recombination lines of hydrogen and helium can also be used to determine the He^+/H^+ ratio. Lockman & Brown (1982) have shown that in some H II regions the abundances determined from these lines have an unusual dependence on quantum number, in the sense that higher n lines tend to give lower helium abundances. To understand this, it is important to identify all of the physical processes which govern the strengths of radio recombination lines. Here we outline one which might account for some of the increase in apparent He/H with decreasing n.

It is usually assumed that the Rydberg levels of hydrogen and helium are affected by collisional/radiative effects in the same way, so that the ratio of ionic abundances is simply the observed ratio of line intensities. For higher n levels which are controlled by collisions and hence are in LTE, this would indeed be the case. On the other hand, for lower levels in which the populations are determined by radiative decays, we show that the radio lines of hydrogen and the helium singlets will be formed under case A conditions, and so will have lower than case B (normally assumed) emissivity. The helium triplets are expected to retain their case B emissivity, since they have no case A–case B distinction. As described below, this could increase the apparent He/H abundance ratio by as much as 25%.

Case B is reached only when Lyman lines scatter often enough to be converted into Balmer lines plus Lyα. For the high-n transitions observed in the radio region this conversion requires of order 10^3 scatterings. The required scatterings might not take place if the lines either escape or are absorbed by dust (Cota & Ferland 1988). For typical velocity fields within H II regions, high-n Lyman lines are blended together and form a "pseudo-continuum" for $n \geq 30$. The absorption oscillator strength for these levels can be expressed as $f \approx 1.1 n^{-3}$ (Allen 1976), and the background opacity (per H^0) due to the integrated oscillator strength of the blended lines is

$$\sigma = \frac{\pi e^2}{mc\,dv} \int_{30}^{\infty} f_{\rm abs}(n)dn \approx 4.4 \times 10^{-18} \text{ cm}^2 \, , \tag{11}$$

i.e., roughly equal to the Lyman continuum photoionization cross section. As described in § 4.3, the grain absorption opacity in the same spectral region is 0.5×10^{-21} cm^2. The ratio of grain absorption to Lyman line opacity, essentially the probability of photon destruction per scattering, is given by

$$X_c = \frac{5 \times 10^{-22} N_{\rm H}}{4.4 \times 10^{-18} N_{\rm H^0}} = 1.1 \times 10^{-4} \frac{N_{\rm H}}{N_{\rm H^0}} \, . \tag{12}$$

For typical conditions within an H II region ($N_{\rm H}/N_{\rm H^0} \approx 10^2 - 10^3$), the parameter is large and Lyman lines are destroyed efficiently; case A is the better approximation for these intermediate-n lines. A similar argument holds true for the helium singlets, except that the hydrogen Lyman continuum opacity effectively destroys the high-n lines, so that case A is reached even for dust-free environments.

Case A is expected to obtain until either n is low enough for Lyman line scattering opacity to be competitive with grain absorption so that case B is reached (this is usually the case for Balmer lines), or n is so large that the level population is controlled by collisions, in which case LTE is expected. In the latter high-n case, hydrogen, the helium singlets, and the helium triplets will all be in LTE, and the relative emissivities will equal the ionic abundance ratio. As n decreases and radiative decays begin to affect the level populations, the hydrogen lines and the helium singlets will approach the (lower) case A emissivities, while the helium triplets, which do not have a case A–case B distinction, remain at the higher emissivity. The ratio of triplet to singlet populations is 3, so that if this effect were overlooked, the helium abundance relative to hydrogen would be overestimated by an amount equal to three-

fourths of the fractional difference between the case A and case B emissivities. This could cause the apparent He/H ratio to increase (with lowering n) by as much as 25% if the levels are well l-mixed.

Although it is straightforward to show that this physics must occur, a quantitative calculation would be quite involved and is beyond the scope of this paper. An exact calculation would need to include the effects of l changing collisions, the distinction between case A and case B being much greater when the levels are l-mixed The effect would be diminished if electron exchange collisions between the triplets and singlets dominate the triplet populations; unfortunately, the needed collision data for this process for high-n levels are not now available. A full treatment would also consider Lyman line scattering with a background continuum. Only then would it be possible to determine the extent to which hydrogen and helium lines differ in emissivity when they are not in LTE.

APPENDIX B

He CHARGE TRANSFER

A correction for collisional excitation of helium lines, using collision data summarized by Clegg (1987), was made in this abundance analysis (§ 3.6). The correction was not large (usually less than 10%), but it is significant, since one hopes to be able to measure helium abundances to a precision better than this.

The collisional contribution depends on both the collision strength for excitation from the metastable $2\,^3S$ level and the population of the level itself (Osterbrock 1988). This in turn is set by the balance between processes which populate it (largely triplet recombinations) and those which depopulate it (electron exchange collisions to the singlets, radiative decays to the ground state, and "other" processes). There have been some recent suggestions that the $2\,^3S$ state actually has a population half that expected by the traditional balance equation (see the papers referenced by Clegg & Harrington 1989). Depletion of the $2\,^3S$ population by ion charge transfer is a suggested explanation (Clegg 1987; Clegg & Harrington 1989), but here we show that the required rate coefficient is unphysically large and that this process is unlikely to affect the level population.

The collisional contribution to the helium lines is largest when the density is highest (Clegg 1987; Osterbrock 1988). In this case, the dominant triplet destruction mechanism is electron exchange collisions to the singlets, with a rate $C_{exc} \approx 3.3 \times 10^{-8}\,N_e\,s^{-1}$ at a temperature of 10^4 K (Osterbrock 1988). If charge transfer with a species N_{trans} is to be competitive with exchange collisions, then it must have a rate coefficient

$$Q_{trans} \geq 3.3 \times 10^{-8}\,\frac{N_e}{N_{trans}}\,cm^3\,s^{-1}\,. \tag{13}$$

If the species N_{trans} is an ion of a heavy element, then the ratio $N_e/N_{trans} \sim 10^4$, and a rate coefficient of $Q_{trans} \geq 3.3 \times 10^{-4}\,cm^3\,s^{-1}$ is needed, nearly five orders of magnitude larger than the rate coefficients for the most favorable reactions.

Clearly charge transfer can be competitive only if the ratio $N_e/N_{trans} \sim 1$, i.e., protons are involved. Energetically, the hydrogen must be left in the $n = 2$ level if the avoided crossing is to occur at a favorable location (Butler & Dalgarno 1980). Charge transfer between protons and excited-state helium is discussed by Janev et al. (1987), who show that this process is not efficient. Either another mechanism affects the population of $2\,^3S$, or the level has the expected population.

APPENDIX C

PHYSICAL PROCESSES INVOLVING GRAINS

The following discussion outlines the changes made to version 76 of the photoionization equilibrium code Cloudy, last described by Ferland (1990), to incorporate some physical processes relating to grains. Two grain populations (species), graphite and an "astronomical silicate," are adopted. Most calculations (like opacity) are based on a realistic power-law size distribution, but in some applications in this paper (where stated) we have calculated only typical quantities (like potential and temperature) rather than quantities for each individual size.

1. GRAIN OPACITY

The optical constants for the grain species are from the calculations of Martin & Rouleau (1990), which extend the work of Draine & Lee (1984) to ionizing energies where the grains are strongly absorbing. The opacity calculations in Martin & Rouleau (1990) were based on the Mathis, Rumpl, & Nordsieck (1977) power-law size distribution to simulate interstellar extinction in diffuse clouds. Similar distributions were considered by Aannestad (1989). As discussed in § 4.3, the dust within the Orion Nebula has a relatively large ratio of total to selective extinction and an exceptionally gray opacity in the ultraviolet, both indicative of a deficiency in small grains and a larger mean grain size. To account for this, we increased the value of the smallest size (g_-) in the size distribution from 0.0025 to 0.03 μm. While this simple adjustment of the size distribution is not entirely adequate for explaining the details of the visible and near-ultraviolet Orion extinction curve (Mathis & Wallenhorst 1981), it should be an improvement for the ionizing ultraviolet portion in which we are most interested.

The extinction properties, both scattering (subscript s) and absorption (subscript a), are shown in Figure 19. The quantities plotted are cross sections (cm^2) per H nucleon: $\sigma = \kappa/N_H$, where κ (cm^{-1}) is the opacity due to grains and N_H (cm^{-3}) is the local density of H in any form. Relative to the diffuse cloud model, the total amount of grain material was preserved, so that σ_a in the infrared and in the extreme ultraviolet and X-ray regions remains unchanged (Fig. 19c). The main differential effect is to lower the cross section through a broad peak at 1 rydberg. There is still a decrease in opacity for energies above the H ionization limit, so that He ionizing photons are less strongly absorbed; this tends to harden the radiation field and, for a given stellar spectrum, bring the He$^+$ and H$^+$ zones into closer correspondence (Aannestad 1989).
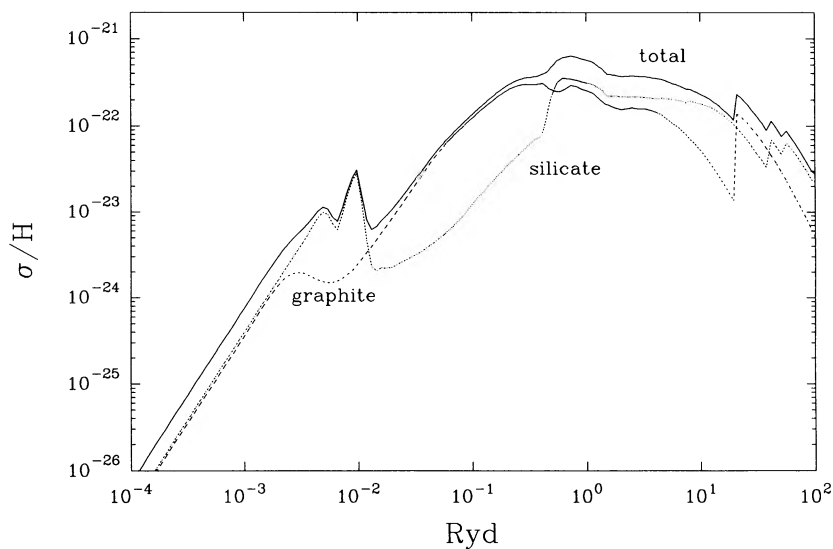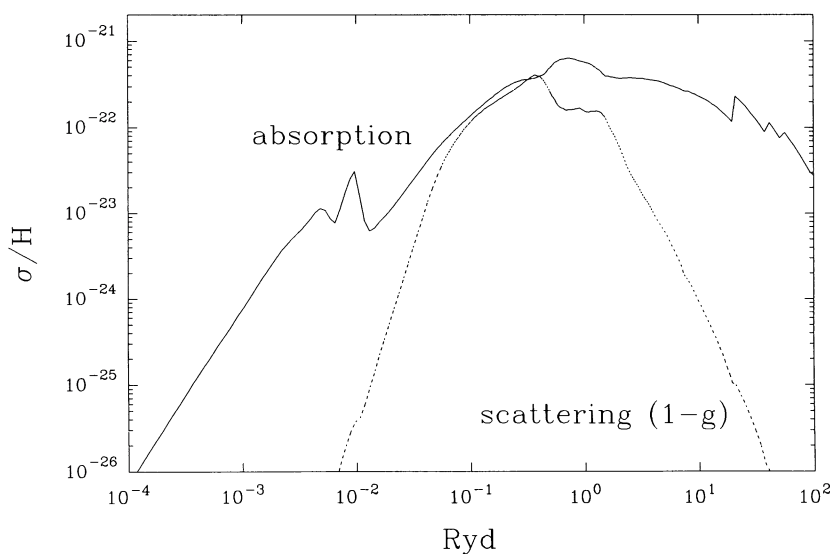
FIG. 19a

FIG. 19b

FIG. 19.—Absorption and scattering cross sections (cm^2 per hydrogen nucleon) for the two grain populations, graphite and silicate. (a) Contribution of graphite and silicates to the total absorption. (b) Total absorption and total effective scattering contributions to the total extinction. To estimate the effective scattering, we have taken the scattering cross section multiplied by $1 - g$, where g is the asymmetry parameter. (c) Comparison of the absorption properties of this mixture with those of the standard ISM.

Rather than σ_s, we plot in Figure 19b an effective scattering cross section $\sigma_{s_e} = \sigma_s(1 - g)$ which discounts the radiation scattered near the forward direction; the asymmetry parameter g approaches unity at high energy, particularly for the larger grains in this model, so that σ_{s_e} becomes much less than σ_a.

The optical depth τ is σ times the H column density (or κ integrated over the path). Absorption attenuates the incident radiation field as $\exp(-\tau_a)$. The effects of scattering are more difficult to model. In an open geometry, scattering attenuates approximately as $(1 + 0.5\tau_{s_e})^{-1}$. However, in a closed geometry, to within factors of order unity, the scattered light is not lost from the beam, and the scattering opacity can be ignored. In either case, τ_{s_e} is fairly small through the ionized nebula. We adopt a closed geometry for the Orion Nebula.

2. DIFFUSE IONIZING RADIATION

A modified version of the "on-the-spot" (OTS) approximation is used in the treatment of sources of diffuse ionizing radiation. Were no other opacity sources present, then, for a closed geometry which is optically thick in the Lyman continuum, all recombinations of hydrogen or helium to the ground state would produce ionizing photons which would be quickly absorbed by other atoms of the recombined species. In this case OTS is an excellent approximation (Van Blerkom & Hummer 1967; Bässgen et al.
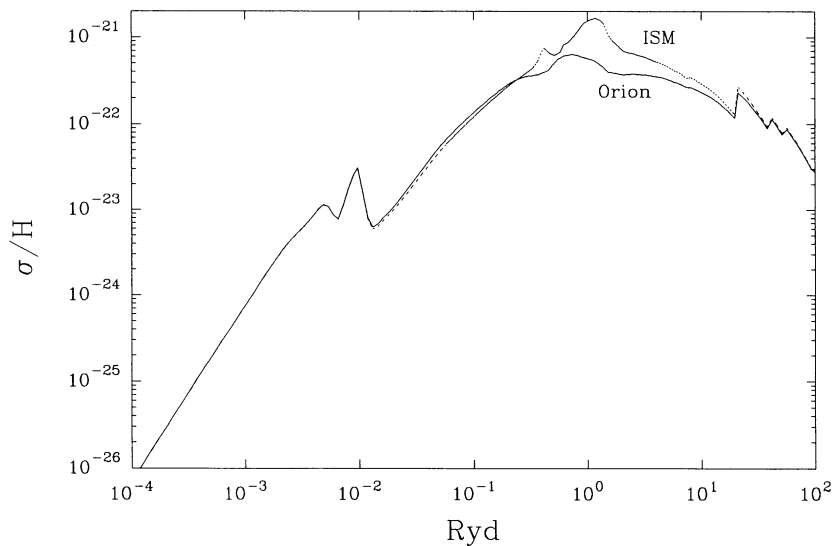
Fig. 19c

1988). However, other opacity sources are present, and these compete in absorbing photons produced by H and He recombinations, making the recombination process more efficient than the OTS approximation would suggest.

The recombination coefficients to the ground and first excited states of hydrogen and helium are modified by the presence of other opacity sources, such as dust, free-free or H^- absorption, and the heavy-element opacities, in the following manner. The net effective recombination rate coefficient $\hat{\alpha}(T_e, n)$ (cm^3 s^{-1}), to level n at electron temperature T_e, is written in terms of the spontaneous radiative recombination rate coefficient $\alpha(T_e, n)$, the escape probability for continuum photons $\beta_c(n)$, and the opacities κ_n and κ_0 for the level n and other opacity sources respectively, as

$$\hat{\alpha}(T_e, n) = \alpha(T_e, n)\left\{\beta_c(n) + [1 - \beta_c(n)]\left(\frac{\kappa_0}{\kappa_0 + \kappa_n}\right)\right\}. \tag{14}$$

In general $\beta_c(n)$ varies between 0 and 0.5 for an optically thick open geometry (see, for example, Davidson 1977), and $\beta_c(n) = 1$ if the gas is optically thin. For an optically thick closed geometry, assumed in the present calculations, we set $\beta_c(1) = 0$ for the ground state of hydrogen and helium, and $\beta_c(2) = 1$ for the Balmer continuum of hydrogen (i.e., the Balmer continuum is optically thin to photoelectric absorption).

These recombination continua produce a flux of on-the-spot photons, ϕ_{OTS} (cm^{-2} s^{-1}), given by

$$\phi_{OTS} = \alpha(T_e, n)N_e N_+\left[\frac{1 - \beta_c(\tau)}{\kappa_0 + \kappa_n}\right], \tag{15}$$

where N_+ is the density of the ion in question. This flux contributes to the ionization and heating of gas and grain constituents.

3. TRAPPED LINE RADIATION

Trapped emission lines (especially Lyα) can be destroyed through absorption by the background opacity. The local destruction of trapped emission lines is determined using the formalism outlined by Netzer, Elitzur, & Ferland (1985). This defines a destruction probability, analogous to the escape probability, in terms of the opacities and line widths. The local flux of OTS photons, accounting for trapping and absorption, is then

$$\phi_{OTS} = \frac{N_u A_{ul} X_C(1 - \beta_{lc})}{\kappa_{total}}, \tag{16}$$

where the symbols are defined in Netzer et al. The total background absorption opacity, κ_{total}, includes photoelectric absorption by ground and excited states of hydrogen and helium and all heavy elements present in the calculation, free-free absorption, and now dust absorption.

4. RADIATIVE ACCELERATION

Although we assume that the emitting region is static, we evaluate the radiative acceleration (cm s^{-2}) due to the direct attenuated continuum flux F. For density ρ this is given by

$$a_{rad} = \frac{1}{\rho c}\int F_\nu \hat{\kappa}_\nu \, d\nu + \frac{1}{\rho c}\sum_l F_\nu(l)\kappa_l B_l \beta_l. \tag{17}$$

Here $\hat{\kappa}$ is the effective continuous opacity; it includes the usual photoelectric and free-free absorption in the gas, and Compton and Rayleigh scattering. In addition, it includes $\kappa_a + (1 - g)\kappa_s$ for the grain contributions, The integral is over all energies considered by the code (from $\lambda \approx 1$ cm to $hv \approx 100$ MeV). The second term is a sum over roughly a dozen strong ultraviolet and optical resonance lines; κ_l is the line opacity, β_l is the Einstein coefficient, and β_l is the escape probability in the direction toward the source of ionizing radiation (Ferland & Rees 1988).

5. PHOTOELECTRIC EMISSION

As discussed below, photoelectric emission from grains contributes directly to heating the gas and, through the grain potential U_g established, affects radiative and collisional heating of the grains and the grain drift velocity. Hence this phenomenon must be included to assess the thermal and dynamical properties of the nebula.

The photoionization rate of a grain, per unit projected area, is

$$\beta_g = \int_{v_0}^{\infty} Q_a \frac{4\pi J}{hv} \hat{Y} \, dv \, , \tag{18}$$

where $\hat{Y}$ is the effective photoelectric yield per absorbed photon, Q_a is the absorption efficiency factor, and $4\pi J/hv$ symbolizes the photon flux of direct, diffuse, and OTS radiation fields. For the OTS line component, the integral is of course just a sum over the line photons that are sufficiently energetic. The threshold for photoemission, to be determined self-consistently, is given by $hv_0 = \max \{V_n + V_g, V_n\}$, where V_n is the photoelectric threshold for a neutral grain and $V_g = eU_g$.

V_g will depend on grain size through Q_a and $\hat{Y}$. In the modeling in this paper, we find a typical V_g for each species by using Q_a averaged over the size distribution: $Q_a = \sigma_a/\Sigma = \kappa_a/N_H \Sigma$. The projected grain area per H, Σ, is similar for each species: 2.1×10^{-22} cm^2 for graphite and 2.4×10^{-22} cm^2 for silicates.

$\hat{Y}$ is constructed as follows. The basic laboratory data measure the yield (per absorbed photon) for a neutral surface, Y_n. For each incident photon energy hv, the photoelectrons emerging from the neutral surface have varying energies E, with a probability distribution $p_n(E)$. To account for electron escape from finite-sized grains, yields measured for semi-infinite sheets in the laboratory have to be corrected by a factor $f(E)$ (which introduces a size dependence). Such a correction would change the shape of the probability distribution as well as increase the integrated emission from a neutral surface (Draine 1978 gives an approximate expression for the overall increase). Then, formally,

$$\hat{Y} = Y_n \int_{E_0}^{hv - V_n} fp_n \, dE \, , \tag{19}$$

where $E_0 = \max (0, V_g)$ introduces the fact that the lowest energy photoelectrons do not escape from positively charged grains.

For the modeling in this paper, we adopt

$$Y_n = \min [Y_0(1 - V_n/hv), Y_1] \tag{20}$$

for $hv \geq V_n$, and we assume $V_n = 8$ eV and $Y_0 = 0.5$ for both grain populations; according to Draine (1978), this combination gives about the right amount of photoelectric emission to heat neutral H I clouds in interstellar space ($hv \leq 13.6$ eV). For the higher energies in H II regions we have introduced a cap at $Y_1 = 0.2$, which is suggested by experimental data. For p_n we adopt a simple form which is independent of E (Draine 1978):

$$p_n = (hv - V_n)^{-1} \, . \tag{21}$$

While only approximate, this induces the physically correct response (decrease) in $\hat{Y}$ (and the photoelectric heating) when the grain is positively charged. Because the form of $f(E)$ is highly uncertain and because the grain population in Orion is deficient in the smallest particles for which any correction f would be most significant, we set $f = 1$ (and again avoided a size dependency). Extension of the flat cap in Y_n to high energies also addresses this issue to some degree. With these assumptions, $\hat{Y}$ is known in analytic form:

$$\hat{Y} = Y_n \min [1, 1 - V_g/(hv - V_n)] \, . \tag{22}$$

6. COLLISIONAL CHARGING OF A GRAIN

Per unit projected area of a grain, collisions with particles of space density N, mass m, and charge Z ($Z = -1$ for electrons) give an effective recombination rate

$$\alpha_g = -N\bar{v}SZ\eta \, , \tag{23}$$

where $\bar{v} = (8kT/\pi m)^{1/2}$ is the mean particle speed. In this expression, and for other collisional rates involving N below, it is implicit that there is a sum of similar terms over all species in the gas. For electrons S is the sticking probability, which we take to be 1 (Spitzer 1948; Watson 1972; Draine 1978). For positively charged nuclei, SZ is the charge transfer efficiency, taken to be Z here. The last factor, η, the correction for Coulomb interactions between the grain and the recombining particles of charge Z, is given in terms of $\phi = ZV_g/kT_e$ by

$$\eta = \begin{cases} 1 - \psi & \text{if } \psi \leq 0 \, , \\ \exp(-\psi) & \text{if } \psi > 0 \, . \end{cases} \tag{24}$$

Terms for positively charged nuclei are included, but are usually small relative to the contribution from free electrons.

7. GRAIN POTENTIAL

The steady state grain potential is determined for each grain species independently by requiring charge balance: $\alpha_g = \beta_g$. Because of the many dependencies on V_g, this is carried out numerically.

8. GRAIN DRIFT VELOCITY

The grain drift velocity is determined by balancing the radiative acceleration due to the direct attenuated radiation field with the drag forces given by equations (1)–(6) of Draine & Salpeter (1979). The equations are solved numerically for the drift velocity, including interactions with electrons and all ions present in the gas.

9. RADIATIVE HEATING AND COOLING OF A GRAIN

Once the grain potential is known, the radiative rate of heating of the grain per unit projected area is

$$G_g(\text{rad}) = \int_0^{v_0} Q_a 4\pi J \, dv + \int_{v_0}^{\infty} Q_a \frac{4\pi J}{hv} (hv - \widehat{EY}) \, dv \; . \tag{25}$$

The last term represents the portion of the photon energy that does not heat the grain but rather passes to the escaping electrons:

$$\widehat{EY} = Y_n \int_{E_0}^{hv - V_n} Efp_n \, dE \; . \tag{26}$$

With the above approximations for f and p_n this is given analytically by,

$$\widehat{EY} = 0.5 Y_n \min \{(hv - V_n), [(hv - V_n)^2 - V_g^2]/(hv - V_n)\} \; . \tag{27}$$

The cooling of a grain by radiative losses, per unit projected area, is given by

$$L_g(\text{rad}) = \int_0^{\infty} Q_a 4\pi B_v(T_g) \, dv \; , \tag{28}$$

where $B_v(T_g)$ is the Planck function for the grain temperature.

10. COLLISIONAL HEATING OF A GRAIN

Collisions with electrons, ions, and neutral particles also heat the grains. Per unit projected area of the grain, this heating rate may be written as

$$G_g(\text{col}) = N\bar{v}S(2kT_e \xi - ZV_g \eta + I\eta - 2kT_g \eta) \; . \tag{29}$$

The first term corresponds to kinetic energy extracted from the gas. The factor ξ makes adjustment for Coulomb interactions and is given by

$$\xi = \begin{cases} 1 - \psi/2 & \text{if } \psi \leq 0 \; , \\ (1 + \psi/2) \exp(-\psi) & \text{if } \psi > 0 \; . \end{cases} \tag{30}$$

The second term in $G_g(\text{col})$ allows for the change of the particle's energy in the grain potential. In the third term, the product SI is the average chemical energy released per impact; here we assume that when impinging ions recombine, the ionization energy released is deposited as heat in the grain (there is then no corresponding term for heating the gas in Λ_g below). The last term describes the effect of thermal evaporation of neutralized ions and thermally accommodated neutral particles (there is no corresponding term for electrons).

In implementing the above processes, S for electrons is again the sticking probability. For positively charged nuclei, S is the energy transfer efficiency, taken here to be unity (this process should be evaluated consistently with that for charge transfer). For neutral particles of mass m striking a grain whose typical atom has mass M, the accommodation coefficient is given by $S \simeq 2mM/(m + M)^2$ (Draine 1978).

11. GRAIN TEMPERATURE

The equilibrium grain temperature is determined by the balance between cooling (L) and heating (G) by radiative and collisional processes. For the radiative terms, we again used Q_a averaged over the size distribution to obtain a typical temperature for each species.

As a test of the bandwidth of the code, and its behavior in a well-defined limit, tests were computed in which the grains were irradiated by blackbody radiation in strict thermodynamic equilibrium (i.e., the color and energy density temperatures were equal). Radiation temperatures between 10 and 10^9 K, the temperature limits to the code, were used. These tests showed that the deduced grain equilibrium temperature was within much better than 1% of the blackbody temperature.

12. PHOTOELECTRIC HEATING OF THE GAS

Heating of the gas by photoemission from grains can be an important process in H II regions (Oliveira & Maciel 1986). For charged grains this heating rate (ergs cm^{-3} s^{-1}) is given by

$$\Gamma_g = \int_{v_0}^{\infty} \kappa_a \frac{4\pi J}{hv} (\widehat{EY} - V_g \hat{Y}) dv \; . \tag{31}$$

The first term describes the energy of the photoelectrons as they leave the surface, balancing the similar term in $G_g(\text{rad})$. The second term compensates for the grain potential and can be seen to balance the related term in $G_g(\text{col})$ when charge balance holds.

13. COLLISIONAL COOLING OF THE GAS

The gas is cooled as the gas particles hit the cooler grain surface. Per unit volume, this cooling rate may be written as

$$\Lambda_g = NN_H \Sigma \bar{v} S(2kT_e \xi - 2kT_g \eta) , \tag{32}$$

the individual terms consistently balancing the corresponding ones in $G_g(\text{col})$.

14. SIMPLE ESTIMATES

Some simple estimates of the effects of embedded grains upon an H II region are given here. The thermal effects of the grains on the gas are potentially powerful, and the net effect can be to either heat or cool the gas.

Grain interactions in the H II region are dominated by grain photoionization balanced by recombination with electrons. The photoionization rate per unit projected area of grain is given by equation (18); for stellar temperatures near 40,000 K, and typical (low) grain potentials and yields, the net photoionization rate is approximately $\beta_b \sim \phi(H)\hat{Y}\bar{Q}_a \sim 0.2Q(H)/4\pi r^2$, where $Q(H)$ is the total number of hydrogen-ionizing photons emitted by the star per second (Osterbrock 1988), and r is the separation between the nebula and the star. Balancing electron recombination (eq. [23]) with grain photoionization, we find a potential of

$$U_g \sim 0.86 t_4 \left(100 \frac{U}{t_4^{1/2}} - 1\right) \text{V} , \tag{33}$$

where the ionization parameter $U \equiv \phi(H)/cN_H$ is the dimensionless ratio of ionizing photons to hydrogen atoms, and $t_4 \equiv T_e/10^4$ K. The ionization parameter of the Orion model was $U \approx 10^{-1.5}$, so that potentials up to ~ 2 V are typical (see Fig. 16e).

We now estimate the thermal effects of the grains on the gas. The local gas hydrogen photoelectric heating rate is

$$\Gamma_H = N_e N_p \alpha_B(T_e)\overline{(h\nu - 13.6 \text{ eV})} , \tag{34}$$

where $\overline{(h\nu - 13.6 \text{ eV})} \approx 5$ eV is the mean energy of a hydrogen photoelectron for a 40,000 K atmosphere, and $\alpha_B(T_e)$ is the case B recombination coefficient. Similarly, the rate at which the grains heat the gas is, for low grain potential,

$$\Gamma_g = \phi(H)\overline{0.5 Y_n(h\nu - V_n)}N_H \sigma_a , \tag{35}$$

where $\sigma_a \sim 5 \times 10^{-22}$ cm^2 is the total grain absorption cross section per hydrogen atom. The ratio of grain to hydrogen photoelectric heating of the gas is then

$$\frac{\Gamma_g}{\Gamma_H} = \frac{Uc\sigma_a}{\alpha_B(T_e)} \frac{0.1\overline{(h\nu - V_g)}}{\overline{(h\nu - 13.6 \text{ eV})}} \approx 12Ut_4^{0.8} \approx 0.4\left(\frac{U}{10^{-1.5}}\right) . \tag{36}$$

The relative importance of Γ_g is confirmed in the detailed model with charged grains (see Fig. 16c).

Grains also cool the gas by capturing electrons. Approximating this rate as

$$\Lambda_g = N_e N_H \sigma \bar{v} 2kT_e(1 - \psi/2) \tag{37}$$

and making use of charge balance for the grain to recast Γ_g, we have a ratio of grain cooling to heating

$$\frac{\Lambda_g}{\Gamma_g} \approx \frac{2kT_e(1 - \psi/2)}{0.5(h\nu - V_n)(1 - \psi)} . \tag{38}$$

We see that grain heating and cooling of the gas are each powerful effects of the same order of magnitude (see also Fig. 16c); their relative size will depend in detail on the hardness of the incident radiation field, the grain potential, and the gas temperature.

REFERENCES

Aannestad, P. A. 1989, ApJ, 338, 162
Adams, W. S. 1944, PASP, 56, 119
Allamandola, L. J., Tielens, A. G. G. M., & Barker, J. R. 1989, ApJS, 71, 733
Allen, C. W. 1976, Astrophysical Quantities (London: Athlone)
Auer, L. H., & Mihalas, D. 1972, ApJS, 24, 193
Bässgen, G., Bässgen, M., & Grewing, M. 1988, A&A, 200, 51
Balick, B., Gammon, R. H., & Hjellming, R. M. 1974, PASP, 86, 616
Balick, B., Gull, T. R., & Smith, M. G. 1980, PASP, 92, 22
Barvainis, R., & Wootten, A. 1987, AJ, 92, 168
Bohlin, R. C., & Savage, B. D. 1981, ApJ, 249, 109
Bohuski, T. J., Dufour, R. J., & Osterbrock, D. E. 1974, ApJ, 188, 529
Boreiko, R. T., Betz, A. L., & Zmuidzinas, J. 1988, ApJ, 325, L47
Breger, M., Gehrz, R. D., & Hackwell, J. A. 1981, ApJ, 248, 963
Brocklehurst, M. 1972, MNRAS, 157, 211
Burke, V. M., Lennon, D. J., & Seaton, M. J. 1989, MNRAS, 236, 353
Burton, M. G., Hollenbach, D. J., & Tielens, A. G. G. M. 1990, ApJ, 365, 620
Butler, S. E., & Dalgarno, A. 1980, ApJ, 241, 838
Cardelli, J. A., & Clayton, G. C. 1988, AJ, 95, 516
Cardelli, J. A., Clayton, G. C., & Mathis, J. S. 1989, ApJ, 345, 245
Castañeda, H. O. 1988, ApJS, 67, 1

Clegg, R. E. S. 1987, MNRAS, 229, 31P
Clegg, R. E. S., & Harrington, J. P. 1989, MNRAS, 239, 869
Conti, P. S. 1971, ApJ, 170, 325
———. 1973, ApJ, 179, 161
———. 1974, ApJ, 187, 539
Cota, S. A., & Ferland, G. J. 1988, ApJ, 326, 889
Cowie, L. L., Songaila, A., & York, D. G. 1979, ApJ, 230, 469
Davidson, K. 1977, ApJ, 218, 20
Davidson, K., & Kinman, T. D. 1985, ApJS, 58, 321
———. 1990, preprint
Dopita, M. A., Dyson, J. E., & Meaburn, J. 1974, Ap&SS, 28, 61
Dorman, B., VandenBerg, D. A., & Laskarides, P. G. 1989, ApJ, 343, 750
Draine, B. T. 1978, ApJS, 36, 595
Draine, B. T., & Lee, H. M. 1984, ApJ, 285, 89
Draine, B. T., & Salpeter, E. E. 1979, ApJ, 231, 77
Elitzur, M., & Ferland, G. J. 1986, ApJ, 305, 35
Ferland, G. J. 1990, OSU Internal Rept. 90-02
Ferland, G. J. & Rees, M. J. 1988, ApJ, 332, 141
Forrest, W. J., Houck, J. R., & Reed, R. A. 1976, ApJ, 208, L133
Franco, J., & Savage, B. D. 1982, ApJ, 255, 541

Gehrz, R. D., Hackwell, J. A., & Smith, J. R. 1975, ApJ, 202, L33
Glassgold, A. E., Huggins, P. J., & Schucking, E. L. 1982, Symposium on the Orion Nebula to Honor Henry Draper (Ann. NY Acad. Sci., Vol. 395)
Goudis, C. 1982, The Orion Complex: A Case Study of Interstellar Matter (Dordrecht: Reidel)
Greve, A., McKeith, C. D., Barnett, E. W., & Gotz, M. 1989, A&A, 215, 113
Grevesse, N., & Anders, E. 1989, in AIP Conf. Proc. 183, Cosmic Abundances of Matter (New York: AIP), 1
Haas, M., Hollenbach, D. J., & Erickson, E. F. 1986, ApJ, 301, L57
Hänel, A. 1977, A&A, 176, 347
Hippelein, H. H., & Münch, G. 1989, A&A, 213, 323
Hummer, D. G., & Storey, P. J. 1987, MNRAS, 224, 801
Janev, R. K., Langer, W. D., Post, D. E., & Evans, K. 1987, Elementary Processes in Hydrogen-Helium Plasmas (Berlin: Springer)
Kaler, J. B. 1976, ApJS, 31, 517
———. 1978, ApJ, 220, 887
Krauss, L. M., & Romanelli, P. 1990, ApJ, 358, 47
Kunasz, P. B., Hummer, D. G., & Mihalas, D. 1975, MNRAS, 202, 92
Kunth, D. 1986, PASP, 98, 984
Kurucz, R. L. 1979, ApJS, 40, 1
———. 1989, private communication
Lockman, F. J., & Brown, R. L. 1982, ApJ, 259, 595
Maciel, W. J., & Pottasch, S. R. 1982, A&A, 86, 380
Martin, P. G., & Rouleau, F. 1990, in Extreme Ultraviolet Astronomy, ed. R. F. Malina & S. Bowyer (Oxford: Pergamon), 341
Martin, P. G., & Whittet, D. C. B. 1990, ApJ, 357, 113
Mathis, J. S., Perinotto, M., Patriarchi, P., & Schiffer, F. H. 1981, ApJ, 249, 99
Mathis, J. S., Rumpl, W., & Nordsieck, K. H. 1977, ApJ, 217, 425
Mathis, J. S., & Wallenhorst, S. G. 1981, ApJ, 244, 483
McCall, M. L. 1979, ApJ, 229, 962
———. 1981, MNRAS, 194, 485
Meaburn, J. 1988, MNRAS, 233, 791
Megeath, S. T., Herter, T., Gull, G. E., & Houck, J. R. 1990, ApJ, 356, 534
Mendoza, C. 1982, in IAU Symposium 103, Planetary Nebulae, ed. D. R. Flower (Dordrecht: Reidel), 261
Mendoza, C., & Zeippen, C. J. 1982, MNRAS, 198, 127
Mihalszki, J. S., & Ferland, G. J. 1983, MNRAS, 205, 1279
Münch, G., & Persson, S. E. 1971, ApJ, 165, 241
Netzer, H., Elitzur, M., & Ferland, G. J. 1985, ApJ, 299, 752
Ney, E. P., & Allen, D. A. 1969, ApJ, 155, L193
Ney, E. P., Strecker, D. W., & Gehrz, R. D. 1973, ApJ, 180, 809
Nussbaumer, H., & Storey, P. J. 1981, A&A, 99, 177
Olive, K. A. 1990, in Proc. Internat. School of Astro-particle Physics (Erice), ed. D. V. Nanopoulos

Oliveira, S., & Maciel, W. J. 1986, A&SS, 126, 211
Osahi, N., Mizuno, A., Tatematsu, K., Sugitani, K., Kasuga, T., & Fukui, Y. 1989, AJ, 97, 458
Osterbrock, D. E. 1988, Astrophysics of Gaseous Nebulae and Active Galactic Nuclei (Mill Valley: University Science Books)
Osterbrock, D. E., & Flather, E. 1959, ApJ, 129, 26
Osterbrock, D. E., Shaw, R. A., & Veilleux, S. 1990, ApJ, 352, 561
Pagel, B. E. J. 1989, in Evolutionary Phenomena in Galaxies, ed. J. E. Beckman & B. E. J. Pagel (Cambridge: Cambridge Univ. Press), 368
Pagel, B. E. J., Terlevich, R. J., & Melnick, J. 1986, PASP, 98, 1005
Pallister, W. S., Perkins, H. G., Scarrott, S. M., Bingham, R. G., & Pilkington, J. D. H. 1977, MNRAS, 178, 93P
Pankonin, V., Walmsley, C. M., & Harwit, M. 1979, A&A, 75, 34
Peimbert, M. 1986, PASP, 98, 1057
Peimbert, M., & Torres-Peimbert, S. 1977, MNRAS, 179, 217
Peimbert, M., Ukita, N., Hasegawa, T., & Jugaku, J. 1988, PASJ, 40, 581
Perinotto, M., & Patriarchi, P. 1980a, ApJ, 235, L13
———. 1980b, ApJ, 238, 614
Rubin, R. H., Simpson, J. P., Erickson, E. E., & Haas, M. R. 1988, ApJ, 327, 377
Savage, B. D., & Jenkins, E. B. 1972, ApJ, 172, 491
Savage, B. D., & Mathis, J. S. 1979, ARA&A, 17, 73
Schiffer, F. H., & Mathis, J. S. 1974, ApJ, 194, 597
Simpson, J. P. 1973, PASP, 85, 479
Simpson, J. P., & Rubin, R. H. 1984, ApJ, 281, 184
Simpson, J. P., Rubin, R. H., Erickson, E. F., & Haas, M. R. 1986, ApJ, 311, 895
Smits, D. P. 1990, Ph.D. thesis, Univ. Capetown
Spitzer, L., Jr. 1948, ApJ, 107, 6
Stoy, R. H. 1933, MNRAS, 93, 588
Tielens, A. G. G. M., & Hollenbach, D. 1985a, ApJ, 291, 722
———. 1985b, ApJ, 291, 747
Torres-Peimbert, S., Peimbert, M., & Daltabuit, E. 1980, ApJ, 238, 133
Turck-Chièze, Cahen, S., Cassé, M., & Doom, C. 1988, ApJ, 335, 415
Van Blerkom, D., & Hummer, D. G. 1967, MNRAS, 137, 353
van der Werf, P. P., & Goss, W. M. 1989, A&A, 224, 209
Watson, W. D. 1972, ApJ, 176, 103
Werner, M. W., Gatley, I., Harper, D., Becklin, E., Loewenstein, R., Telesco, C., & Thronson, H. 1976, ApJ, 204, 420
White, R. L., Schiffer, F. H., & Mathis, J. S. 1980, ApJ, 241, 208
Wilson, O. C. 1937, PASP, 49, 338
Wilson, T. L., & Pauls, T. 1984, A&A, 138, 225
Yorke, H. W. 1986, ARA&A, 24, 49
Zuckerman, B. 1973, ApJ, 183, 863